Journal of the American Helicopter Society, Volume 61, Number 3, July 2016, pp. 1-16
DOI:10.4050/JAHS.61.032010

An Improved Analytical Approach for Modeling the Effect of Rotor Wake Curvature using Finite-State Induced Flow Models

Ioannis Goulos [1]

Propulsion Engineering Centre, Cranfield University

School of Aerospace, Transport, and Manufacturing

Bedfordshire, MK430AL, United Kingdom

Abstract

This paper presents an analytical formulation capable of modeling the effect of wake curvature on the dynamic response of helicopter rotors for flight dynamics applications. The classical solution of potential flow derived for a curved vortex tube is utilized. The existing solution is generalized to account for an arbitrary distribution of circulatory disk loading. An orthogonality analysis is carried out to obtain a finite set of inflow perturbation coefficients that describe the aerodynamic effect of wake curvature in a generalized manner. The obtained coefficients are superimposed upon an existing finite-state induced flow model that assumes a skewed, non-curved cylindrical wake. The developed approach is coupled with an unsteady blade element aerodynamics model, a rotor blade structural mechanics model, and a nonlinear rotor dynamics model. The overall method is initially employed to assess the effect of wake curvature on the dynamic response of a small-scale articulated rotor with a flap frequency ratio equal to unity. Subsequently, the integrated model is deployed to investigate the influence of wake curvature on the predicted stability and nonlinear control response of a hingeless rotor helicopter. It is shown that inclusion of the wake curvature effect is essential for predicting the pitch–roll off-axis response of the investigated aircraft. Good agreement is demonstrated between the derived model and nonlinear predictions carried out by resolving the complex wake geometry. The developed approach is an improved, time-accurate method applicable to hover and forward flight.

JAHS-1822-May-2015

[1]Research Fellow, Corresponding author; email: i.goulos@cranfield.ac.uk

Published by Vertical Flight Society. This is the Author Accepted Manuscript issued with: Creative Commons Attribution Non-Commercial License (CC:BY:NC 4.0). The final published version (version of record) is available online at DOI:10.4050/JAHS.61.032010. Please refer to any applicable publisher terms of use.

Nomenclature

Roman Symbols

$[C]$	Wake curvature influence matrix (Krothapalli model)
$[C]^{r,m}_{j,n}$	Partitions comprising the overall inflow gain perturbation matrices
$[D]_{0,1,2}$	Inflow gain perturbation matrices associated with the effect of rotor wake curvature
$[L^c]$, $[L^s]$	Cosine and sine inflow gain matrices
$[M^c]$, $[M^s]$	Cosine and sine apparent mass matrices
$[V^c]$, $[V^s]$	Cosine and sine mass flow parameter matrices
$\bar{P}^m_n(\nu)$	Normalized associated Legendre function of first kind
$\bar{q}$, $\bar{p}$	Normalized pitch and roll rates, $= \dfrac{q}{\Omega}, \dfrac{p}{\Omega}$
$\bar{r}$	Normalized radial coordinate on the rotor disk, $= \dfrac{r}{R}$, non-dimensional
$\bar{r}_0$	Normalized vortex tube radius, non-dimensional
$\bar{t}$	Non-dimensional time, $= \Omega t$
$\Delta u(\bar{r}, \psi)$	Normalized induced flow perturbations due to a curved vortex tube, non-dimensional
$\hat{r}$	Ratio of normalized radial coordinate to vortex tube radius, $= \dfrac{\bar{r}}{\bar{r}_0}$, non-dimensional
τ^{mc}_n, τ^{ms}_n	Cosine and sine generalized aerodynamic pressure coefficients
$a_n(\bar{r})$, $b_n(\bar{r})$	Integral radial functions employed in the generalized vortex tube model, non-dimensional
$c^{1-4}_n(\bar{r})$, $d^{1-3}_n(\bar{r})$	Integral radial functions employed in the generalized vortex tube model, non-dimensional
$e^{1,2}_n(\bar{r})$, $f^{1,2}_n(\bar{r})$	Integral radial functions employed in the generalized vortex tube model, non-dimensional
$e_i(\hat{r})$, $d_i(\hat{r})$	Curved vortex tube geometric influence coefficients, $i = 1, \cdots 6$, non-dimensional
K_{Re}	Wake curvature parameter, non-dimensional
r, R	Local radial coordinate and rotor disk radius, m
S	State of wake spacing, $= 2\pi V_T$
t	Time, sec
V, V_T	Flow parameter and total normalized flow on the rotor disk plane, non-dimensional
V_n, V_p	Free-stream velocity components normal and parallel to the rotor disk, m/sec
X	Function of wake skew angle, $= \tan\lvert\chi/2\rvert$

Greek Symbols

α_j^r, β_j^r	Non-dimensional wake-induced flow expansion coefficients, non-dimensional
$\bar{\Gamma}(\bar{r}, \psi)$	Normalized circulatory loading distribution on the rotor disk, non-dimensional
$\bar{\Gamma}_0$, $\bar{\Gamma}_{1c}$, $\bar{\Gamma}_{1s}$	Mean and first harmonic azimuthal components of rotor bound circulation, non-dimensional
$\bar{\gamma}_0$, $\bar{\gamma}_{1c}$, $\bar{\gamma}_{1s}$	Mean and first harmonic components of vorticity density of a vortex tube, non-dimensional
β_0, β_{1c}, β_{1s}	Rotor coning, longitudinal, and lateral flapping angles, rad
χ	Wake skew angle, $= \pi/2 - \arctan\lvert\frac{\lambda_f + \lambda_m}{\mu}\rvert$, rad
$\Delta\alpha_j^r$, $\Delta\beta_j^r$	Normalized cosine/sine flow perturbations due to wake curvature, non-dimensional
$\Delta\lambda(\bar{r}, \psi)$	Normalized flow perturbations due to a curved generalized vortex tube, non-dimensional
η, ν	Ellipsoidal coordinates, non-dimensional
κ_c, κ_s	Longitudinal and lateral wake curvature values, non-dimensional
$\lambda(\bar{r}, \psi, \bar{t})$	Non-dimensional wake-induced velocity at the rotor disk
λ_f	Normalized free-stream velocity normal to the rotor disk, $= \frac{V_n}{\Omega R}$
λ_m	Normalized mean wake-induced velocity normal to the rotor disk, $= \sqrt{3}\alpha_1^0$
μ	Normalized free-stream velocity parallel to the rotor disk, $= \frac{V_p}{\Omega R}$
ν_β	Rotor flap frequency ratio, non-dimensional
Ω	Rotor speed, rad/sec
$\phi_n^m(\bar{r})$	Induced flow expansion functions, $= \bar{P}_n^m(\nu)/\nu$, $\nu = \sqrt{1 - \bar{r}^2}$
ψ	Azimuthal coordinate on the rotor disk, rad
ρ	Air density, kg/m^3
τ_X, τ_S, τ_R	Time-constants of dynamic wake skew, vortex spacing, and wake curvature

Superscripts

$\dot{()}$, $()'$	First derivatives with respect to non-dimensional time $\bar{t}$ and disk radius $\bar{r}$, respectively
$()^{cc,cs,sc,ss}$	Denoting the coupling between the cosine/sine parts of perturbed rotor inflow and the cosine/sine parts of aerodynamic pressure on the rotor disk, respectively
$()^{mean/cyc}$	Denoting the induced flow perturbations of a curved vortex tube to the mean/cyclic variations of circulatory loading on the rotor disk, non-dimensional
$()^{r,m}$	Harmonic number indices

Subscripts

$()_{\hat{r}\leq 1}$, $()_{\hat{r}\geq 1}$	Denoting the integration domains corresponding to $\hat{r} \leq 1$ and $\hat{r} \geq 1$, respectively
$()_{c,s}$	Denoting the inflow perturbations due to the effect of longitudinal/lateral wake curvature
$()_{cX,sX}$	Denoting linear coupling between longitudinal/lateral wake curvature and wake skew
$()_{cX^2,sX^2}$	Denoting quadratic coupling between longitudinal/lateral wake curvature and wake skew
$()_{j,n}$	Legendre function polynomial number indices
$()_{qs}$	Referring to a quasi-steady state

Introduction

Background

The main rotor of a helicopter acts as a lifting, propulsive, and control device simultaneously. For this reason it is generally accepted that flight dynamics simulation must not only cater for accurate predictions of rotor power and thrust, but it must also provide precise estimates of the time-dependent rotor forces and moments exerted on the aircraft fuselage. Especially considering cases where higher-frequency harmonic content is desirable in the analysis, it is essential that the dynamic behavior of the flexible rotor blades is accurately predicted. This not only requires sophisticated models for structural and rotor dynamics, but also entails advanced modeling fidelity in terms of rotor inflow and blade aerodynamics.

The dynamic response of the main rotor is strongly coupled with the encountered flow-field conditions. Hence, accurate simulation of helicopter flight dynamics requires that the nature of the surrounding complex flow-field is thoroughly understood and modeled at an acceptable level of detail. The fidelity of the approach may depend on application requirements and is usually limited by the associated computational cost. Investigations focusing on the underlying physics of the three-dimensional rotor inflow may require a rather sophisticated modeling approach. This may possibly include the employment of free-wake vortex filament methods (Ref. 1), vorticity transport simulation (Ref. 2), or maybe even a viscous Computational Fluid Dynamics (CFD) analysis (Ref. 3). However, with respect to real-time flight dynamics applications, a more computationally efficient modeling approach may be desired.

The rotor wake is the major contributing factor that affects the overall induced flow-field. Significant work has been done to date on modeling the induced flow arising from the rotor wake at various levels of fidelity. The majority of comprehensive rotorcraft codes (UMARC, CAMRAD/JA, CAMRAD II, S4,

RCAS, DYMORE, and HOST) (Ref. 4) incorporate free-wake modeling to predict the wake-induced flow at the rotor tip-path plane. Free-wake models (Refs. 1, 5, 6) solve for the wake geometry directly and are formulated based predominantly on first principles with limited reliance on experimental data. They resolve certain wake distortion parameters such as curvature, skewness, vortex spacing, and tip-vortex roll-up through using a discretized, time-dependent, three-dimensional representation of the wake. However, if not properly refined, they can be prone to numerical errors due to the spatial discretization of the wake. Furthermore, real-time execution can be hindered by the relatively large associated computational cost.

Finite-state induced flow models

Although the implementation of free-wake models in real-time flight simulation has been investigated with encouraging results (Ref 7), nonlinear flight dynamics applications generally employ some variation of a finite-state induced flow model (Refs. 8, 9). These models have emerged within the last couple of decades as a compromise between simulation fidelity and computational efficiency. Finite-state induced flow models were designed predominantly for real-time flight simulation (Ref. 10). They employ a continuous and dynamic wake representation without any geometric discretization errors. The vortical wake is modeled as a skewed cylinder without accounting for the effect of self-induced wake roll-up. The induced flow at the rotor disk is expressed as a function of a number of flow-states determined by the solution of a first-order ordinary matrix differential equation. Hence, due to their simplicity, they lend themselves to real-time execution. However, their physical accuracy is dependent on the selected number of flow-states.

The most popular finite-state inflow model is that of Peters and He (Refs. 8,9) which is an extrapolation of the linear, three-state dynamic inflow theory of Pitt and Peters (Ref. 11). Peters and He were able to extend Pitt's original first harmonic inflow model with the inclusion of higher-frequency harmonic content along with refined expressions for the radial distribution of inflow using normalized associated Legendre functions $\bar{P}_j^r(\nu)$, $\nu = \sqrt{1-\bar{r}^2}$. Hence, they were able to derive a completely generalized dynamic wake model entirely in closed form, capable of providing time-accurate estimates of the three-dimensional wake-induced flow. Within the Peters and He model, the normalized induced flow $\lambda(\bar{r}, \psi)$ at the rotor disk is expressed as the sum of an unlimited number of harmonics and radial shape functions, as follows:

$$\lambda(\bar{r}, \psi, \bar{t}) = \sum_{r=0}^{\infty} \sum_{j=r+1,\ r+3,\ldots}^{\infty} \phi_j^r(\bar{r})[\alpha_j^r(\bar{t}) \cos r\psi + \beta_j^r(\bar{t}) \sin r\psi] \tag{1}$$

where $\phi_j^r(\bar{r}) = \bar{P}_j^r(\nu)/\nu$. The model's flow states essentially correspond to the time-dependent coefficients for the cosine and sine terms on the Right-Hand Side (RHS) of Eq. (1), $\alpha_j^r(\bar{t})$ and $\beta_j^r(\bar{t})$, respectively. These are determined by the solution of the following uncoupled systems of first-order ODEs:

$$[M^c]\{\dot{\alpha}_j^r\} + [V^c][L^c]^{-1}\{\alpha_j^r\} = \frac{1}{2}\{\tau_n^{mc}\} \tag{2a}$$

$$[M^s]\{\dot{\beta}_j^r\} + [V^s][L^s]^{-1}\{\beta_j^r\} = \frac{1}{2}\{\tau_n^{ms}\} \tag{2b}$$

where $[M^c]$ and $[M^s]$ are the apparent mass matrices that contain the time-constants associated with the cosine and sine matrix ODEs described by Eq. (2a) and Eq. (2b), respectively. Similarly, $[L^c]$ and $[L^s]$ are the cosine and sine inflow gain matrices, respectively. These depend only on the wake skew parameter X, ($X = \tan|\chi/2|$, where χ is the wake skew angle), whilst $[V^c]$ and $[V^s]$ denote the mass flow parameter matrices for the corresponding parts of the matrix ODEs. The pressure coefficients in the RHS of Eqs. (2a, 2b), $\{\tau_n^{mc}\}$ and $\{\tau_n^{ms}\}$, are user-supplied time-dependent integrals denoting the generalized aerodynamic forces. These depend only on the circulatory blade lift and can be obtained using any aerodynamic theory.

However, it is noted that within Eqs. (2a, 2b) the rotor wake is implicitly treated as a skewed cylinder without any account for wake distortion effects such as curvature, vortex spacing, or wake roll-up. Further elaboration on the theoretical development and validation of finite-state induced flow models, as well as a comprehensive description of the current "state of the art" has been provided in Ref. 10.

Rotor wake curvature and off-axis response

Finite-state induced flow models were quickly established in the field of flight simulation as reliable, robust, and efficient tools for the numerical prediction of wake-induced flow (Ref. 10). However, correlations with flight test data revealed that the physical behavior that the rotor wake exhibited during maneuvering flight, was not adequately captured by the existing finite-state models (Ref. 12). The discrepancies between predictions and measured data were particularly apparent with regards to the pitch–roll off-axis coupling characteristics. It is well known that for a typical helicopter pull-up maneuver using cyclic control inputs, there is inevitably an associated roll response (an off-axis response) and vice versa. However, flight simulation codes that utilized the Peters–He and Pitt-Peters induced flow models, consistently predicted the off-axis rotor response to be of opposite sign from that suggested by flight test data.

Rosen and Isser (Ref. 13) postulated that the aforementioned discrepancies between theoretical predictions and measured data may originate in the effective curvature of the wake during maneuvering flight.

The effective curvature of the wake is illustrated in Fig. 1 for near-hover maneuvering flight. Due to the pitch–roll angular motion of the shaft, the rotor wake distorts into a curved helix. Hence, the blade tip-vortices effectively pile-up more tightly beneath one semicircle of the rotor disk, while synchronously expand more quickly downstream of the blades on the opposite side of the disk. This leads to first harmonic inflow gradients that produce a cyclic pitch effect, thus forcing the blades close to their fundamental flap frequency. The blades respond to once-per-rev (1P) harmonic forcing with a phase lag of approximately 90°, therefore generating hub moments in an off-axis manner. Rosen and Isser demonstrated that a simple curved vortex-wake model could indeed improve the predictions of the off-axis rotor response.

Krothapalli *et al.* (Refs. 14, 15) performed an extensive analytical investigation considering the effect of quasi-steady rotor wake curvature on the off-axis rotor response during maneuvering flight. Eventually, they were able to extend the generalized dynamic wake model developed by Peters and He to include the lower-frequency effects of quasi-steady wake curvature for hovering flight conditions with zero wake skew angle (Ref. 15). The augmented finite-state inflow model was presented in the following form:

$$\begin{bmatrix} [M^c] & [0] \\ [0] & [M^s] \end{bmatrix} \begin{Bmatrix} \dot{\alpha}_j^r \\ \dot{\beta}_j^r \end{Bmatrix} + \begin{bmatrix} [V^c] & [0] \\ [0] & [V^s] \end{bmatrix} \left\{ \begin{bmatrix} [L^c] & [0] \\ [0] & [L^s] \end{bmatrix} + K_{Re}\,[C] \right\}^{-1} \begin{Bmatrix} \alpha_j^r \\ \beta_j^r \end{Bmatrix} = \frac{1}{2} \begin{Bmatrix} \tau_n^{mc} \\ \tau_n^{ms} \end{Bmatrix} \tag{3}$$

where the matrices $[M^{c/s}]$, $[L^{c/s}]$, $[V^{c/s}]$ are the original apparent mass, inflow gain, and mass flow parameter matrices, in that order, as employed in Eqs. (2a, 2b) of the original Peters and He model. The terms K_{Re} and $[C]$ essentially denote the wake curvature parameter (Ref. 15) and the corresponding matrix of influence coefficients, respectively. The wake curvature influence matrix $[C]$ depends only on the quasi-steady longitudinal and lateral wake curvature values, κ_c and κ_s, respectively. These are defined as:

$$(\kappa_c)_{qs} = \frac{\bar{q} - \bar{\dot{\beta}}_{1c}}{\lambda_m + \lambda_f} \tag{4}$$

$$(\kappa_s)_{qs} = \frac{\bar{p} - \bar{\dot{\beta}}_{1s}}{\lambda_m + \lambda_f} \tag{5}$$

where $\bar{q} = \dfrac{q}{\Omega}$ and $\bar{p} = \dfrac{p}{\Omega}$ signify the normalized pitch and roll rates, respectively. $\bar{\dot{\beta}}_{1c} = \dfrac{\dot{\beta}_{1c}}{\Omega}$ and $\bar{\dot{\beta}}_{1s} = \dfrac{\dot{\beta}_{1s}}{\Omega}$ correspond to the normalized rates of first harmonic flapping, whilst the subscript $()_{qs}$ denotes quasi-steady conditions. The symbols λ_m and λ_f refer to the normalized mean induced flow and free-stream velocity normal to the rotor disk, respectively. The wake curvature influence matrix $[C]$ was derived in Ref. 15 for hovering flight ($\chi = 0^\circ$) and an arbitrary disk loading. In order to do so, Krothapalli

modeled the curved rotor wake as an infinite series of concentric, un-contracted vortex tubes, starting from the blade root and reaching up to the disk edge. The effect of quasi-steady wake curvature was then investigated analytically by applying vortex tube theory to the curved wake geometry.

It is important to observe in Eq. (3) that, after including the effect of wake curvature in the overall finite-state model, the inflow gain matrices obtained from the original Peters–He formulation, $[L^c]$ and $[L^s]$, were now combined into a single, partitioned inflow gain matrix. This was due to the fact that wake curvature essentially introduced a coupling between the mean disk loading and the longitudinal as well as lateral variations of rotor inflow. It is emphasized that in the original model of Peters and He (Eqs. (2a, 2b)), coupling existed only between the mean disk loading and the longitudinal gradient of inflow which was due to a non-zero wake skew angle in forward flight. The Krothapalli wake curvature augmentation method neglects any coupling between wake curvature and wake skew and assumes negligible azimuthal variations of circulatory disk loading. Furthermore, it is limited to first harmonic variations of induced flow without accounting for higher-order harmonic content in the inflow response. Thus, its applicability is limited to low-frequency flight dynamics applications as well as hovering flight conditions.

Prasad *et al.* (Ref. 16) showed that in the same way that dynamic inflow incurs a first-order time-delay in the development of the quasi-steady wake-induced flow-field, the effects of longitudinal and lateral wake curvature (κ_c and κ_s), along with vortex spacing $S = 2\pi V_T$ and wake skew X, also exhibit first-order behavior with respect to non-dimensional time. Hence, as long as the corresponding time-constants could be extracted from an adequate aerodynamic theory, their time-dependent nature could be modeled using a system of first-order ODEs. Subsequently, Zhao *et al.* (Ref. 17) employed a numerical approach based on vortex tube analysis to extract the respective time-delays for the aforementioned wake distortion parameters. In doing so, they developed the following four-state reduced order model:

$$\begin{bmatrix} \tau_X & 0 & 0 & 0 \\ 0 & \tau_S & 0 & 0 \\ 0 & 0 & \tau_R & 0 \\ 0 & 0 & 0 & \tau_R \end{bmatrix} \begin{Bmatrix} \dot{X} \\ \dot{S} \\ \dot{\kappa}_c \\ \dot{\kappa}_s \end{Bmatrix} + \begin{Bmatrix} X \\ S \\ \kappa_c \\ \kappa_s \end{Bmatrix} = \begin{Bmatrix} X \\ S \\ \kappa_c \\ \kappa_s \end{Bmatrix}_{qs} \tag{6}$$

where τ_X, τ_S, and τ_R are the time-constants associated with the dynamic behavior of wake skew, vortex spacing, and wake curvature, respectively. These were provided by Zhao *et al.* in Ref. 18.

Scope of present work

Zhao *et al.* (Ref. 18) also noted the extension of the augmented Peters–He finite-state induced flow model to the forward flight case, along with the inclusion of aerodynamic coupling between wake curvature and skew, as well as higher-order harmonic content in the inflow response. However, the authors of Ref. 18 only briefly touched on the the particular aspect of rotor wake modeling without elaborating further on the underlying theoretical background or the necessary mathematical manipulations for the extension of the model. Furthermore, they did not explicitly provide analytical expressions for the mathematical augmentation of the original model of Peters and He in order to cater for the effect of rotor wake curvature in forward flight with non-zero wake skew, as was done by Krothapalli *et al.* (Ref. 15) for the case of an un-contracted stream-tube at hovering flight conditions.

In light of the existing literature, the general scope of this work is to develop an improved mathematical formulation for the augmentation of the original Peters–He induced flow model, to include the effect of wake curvature in hover and forward flight. The developed approach accounts for the dominant effects associated with the aerodynamic coupling between wake curvature and skew. Furthermore, it caters for the previously omitted circumferential variations of circulatory disk loading along with the higher-frequency harmonic content in the inflow response. The proposed model aims to extend the applicability of the original finite-state model of Peters and He, not only to a wider range of operating regimes, but also towards higher-frequency flight dynamics applications, such as the design of hingeless, bearingless, or Higher-Harmonic Control (HHC) systems. The specific objectives of this paper can be outlined as follows:

1) To present a thorough modeling approach based on potential flow, regarding the effect of wake curvature on the fundamental and higher-order harmonic characteristics of rotor inflow, including the aerodynamic coupling between wake curvature and skew.

2) To provide a series of analytical expressions for the augmentation of the finite-state induced flow model of Peters and He in order to include the effect of wake curvature in hover and forward flight.

3) To assess the effect of rotor wake curvature on the dominant stability derivatives associated with the pitch–roll off-axis response characteristics of a representative helicopter in forward flight.

4) To evaluate the accuracy of the proposed mathematical formulation compared to that of existing approaches, in terms of capturing the pitch–roll off-axis response characteristics of a representative helicopter operating at near-hover and forward flight conditions.

The mathematical model for the treatment of rotor wake curvature presented in this paper is broadly arranged as follows; The classical solution of incompressible potential flow derived for a curved vortex tube of uniform vorticity strength is employed. The existing curved vortex tube analysis is mathematically generalized to account for arbitrary radial and circumferential variations of circulatory disk loading. An orthogonality analysis is carried out on the derived curved vortex wake model for the general case of an arbitrary distribution of disk loading. The radial distribution of aerodynamic pressure is expressed as a finite series of normalized associated Legendre functions whilst a Fourier series is employed for the expansion of circumferential variations. This leads to a set of integral functions that describe the inter-harmonic coupling between the inflow perturbations on the rotor disk and the respective variations of circulatory disk loading. The linear character of incompressible potential flow allows for the obtained coefficients to be superimposed on existing finite-state inflow models (Refs. 8, 9) that assume a skewed, non-curved cylindrical wake representation. The end result is an augmented induced flow formulation that includes the effect wake curvature and is applicable to the general case of non-zero wake skew angle.

The developed mathematical model for fluid mechanics is coupled with an unsteady blade element aerodynamics model, a rotor blade structural mechanics model, and a nonlinear rotor dynamics model. The combined formulation is implemented in an existing framework for helicopter flight mechanics. The integrated approach is initially deployed to investigate the effect of wake curvature on the dynamic response of a small-scale articulated rotor model with a flap frequency ratio equal to unity. A comparative evaluation is carried out for hovering conditions between predictions made with the newly-developed theory and the existing model of Krothapalli (Ref. 15). Subsequently, the integrated approach is deployed to investigate the influence of wake curvature on the flight dynamics of a hingeless rotor helicopter modeled after the MBB Bo 105 helicopter. Results are presented in terms of stability derivatives and nonlinear control response characteristics. Extensive comparisons are carried out with flight tests measurements as well as with numerical predictions carried out through resolving the complex wake geometry.

Mathematical Formulation

Baseline vortex tube analysis

The implicit coupling between the characteristics of rotor disk loading and the associated inflow perturbations due to the effect of wake curvature have been evaluated analytically in Ref. 18 for a single vortex tube of radius $\bar{r}_0$. The methodology of Ref. 18 assumes that the vortices generated at the blade tips are wrapped around a continuous surface of concentrated vorticity. This surface denotes the outer boundary of the rotor wake. The induced flow across the rotor disk is then calculated by applying the Biot–Savart law through invoking the classical assumption of incompressible and inviscid flow. The formulation presented in this paper is based on the original vortex tube analysis described in Ref. 18. Therefore, only a brief overview of the most important features of the original theory will be dealt with in this subsection.

Expressing the azimuthal variation of rotor bound circulation $\bar{\Gamma}(\psi)$ in terms of a Fourier series that reaches only up to the first harmonic components of disk loading, results in the following expression:

$$\bar{\Gamma}(\psi) = \bar{\Gamma}_0 + \bar{\Gamma}_{1c}\cos\psi + \bar{\Gamma}_{1s}\sin\psi \tag{7}$$

where $\bar{\Gamma}_0$ is the mean rotor bound circulation, whilst $\bar{\Gamma}_{1c}$ and $\bar{\Gamma}_{1s}$ denote the longitudinal and lateral azimuthal variations of circulatory disk loading, respectively. The mean and first harmonic cyclic components of vorticity strength with respect to the resulting vortex tube ($\bar{\gamma}_0$, $\bar{\gamma}_{1c}$, and $\bar{\gamma}_{1s}$), can be related to their reciprocal values of blade bound circulation ($\bar{\Gamma}_0$, $\bar{\Gamma}_{1c}$, and $\bar{\Gamma}_{1s}$) as shown below:

$$\bar{\gamma}_0 = \frac{\bar{\Gamma}_0}{V_T} \tag{8}$$

$$\bar{\gamma}_{1c} = \frac{\bar{\Gamma}_{1c}}{V_T} \tag{9}$$

$$\bar{\gamma}_{1s} = \frac{\bar{\Gamma}_{1s}}{V_T} \tag{10}$$

where $V_T = \sqrt{\mu^2 + (\lambda_f + \lambda_m)^2}$ essentially denotes the mass flow parameter associated with the normalized free-stream velocity components (λ_f and μ) and the mean wake-induced flow λ_m.

The author of Ref. 18 was able to extrapolate the analysis presented in Ref. 16 in order to derive closed form expressions for the mean and cyclic components of inflow perturbations due to a single, quasi-steadily curved, and simultaneously skewed vortex tube of radius $\bar{r}_0$. In order to account for the effects related to both mean and first harmonic cyclic components of circulatory loading, Ref. 18 employed a geometric configuration comprising a total of five vortex tubes, as demonstrated in Fig. 2(a). The principle of superposition was subsequently invoked in order to mathematically sum the inflow perturbations arising separately due to the stength of the vorticity carried by each of the assumed vortex tubes.

Figure 2 shows that in order to model the inflow perturbations on the rotor disk due to the effect of mean bound circulation $\bar{\Gamma}_0$, a single vortex tube of radius $\bar{r}_0$ and circumferentially uniform vorticity strength $\bar{\gamma}_0$ was employed. This cylindrical surface of vorticity was assumed to be quasi-steadily curved with κ_c, κ_s being the respective values of longitudinal and lateral wake curvature, and to also employ a wake skew parameter X in the longitudinal direction. After a series of mathematical manipulations, the associated inflow perturbations were expressed in a completely closed form as follows:

$$\Delta u^{mean}(\bar{r},\psi) = -\left\{\begin{array}{ll} \frac{\bar{\gamma}_0}{2}\kappa_c X\bar{r}_0 e_1(\hat{r}) + \frac{\bar{\gamma}_0}{2}\bar{r}_0 X e_2(\hat{r})[\kappa_c\cos 2\psi + \kappa_s \sin 2\psi] + & \\ \frac{\bar{\gamma}_0}{2}\kappa_c\bar{r}[1-\frac{3}{2}X^2]\cos\psi + \frac{\bar{\gamma}_0}{2}\kappa_s\bar{r}[1+\frac{3}{2}X^2]\sin\psi & (\hat{r}<1) \\ & \\ \frac{\bar{\gamma}_0}{2}\kappa_c X\bar{r}_0 e_3(\hat{r}) + \frac{\bar{\gamma}_0}{2}\bar{r}_0 X e_4(\hat{r})[\kappa_c\cos 2\psi + \kappa_s \sin 2\psi] + & \\ \frac{3\bar{\gamma}_0}{4}\bar{r}_0 X^2 e_5(\hat{r})[\kappa_c\cos\psi + \kappa_s\sin\psi] + & \\ 3\frac{\bar{\gamma}_0}{4}\bar{r}_0 X^2 e_6(\hat{r})[\kappa_c\cos 3\psi + \kappa_s\sin 3\psi] & (\hat{r}>1) \end{array}\right\} \tag{11}$$

The superscript $()^{mean}$ signifies that the specific inflow perturbations are due to the effect of mean disk loading, $\hat{r} = \dfrac{\bar{r}}{\bar{r}_0}$, whilst $\bar{r}$ and ψ denote the radial and azimuthal coordinates across the rotor disk, as shown in Fig. 2(b). The symbols $e_i(\hat{r}),\ i = 1, 2, ...6$ are geometric influence coefficients that depend only on the vortex tube geometry. These were provided in analytical closed-form by Zhao in Ref. 18.

The negative sign in front of the RHS of Eq. (11) has been added to maintain consistency in the convention used to specify the positive direction of induced flow. The notation employed in the context of this work dictates that a positive inflow perturbation $\Delta u(\bar{r},\psi)$ represents a downwash, while the opposite holds true for an upwash. This is the generally accepted convention used in induced flow modeling. However, the closed form expressions of Ref. 18 correspond to the velocity components normal to the rotor disk, expressed in the Cartesian system. As such, they are positive for upward flow and vice versa.

Regarding the inflow perturbations associated with the first harmonic longitudinal ($\bar{\Gamma}_{1c}$) and lateral ($\bar{\Gamma}_{1s}$) variations of circulatory loading, an analytical approach was proposed in Ref. 18 similar to that developed by Dress in Ref. 19. With respect to the longitudinal harmonic component, two hypothetical vortex tubes of radius $\dfrac{\bar{r}_0}{2}$ were positioned anti-diametrically as shown in Figs. 2(a) and (b). Their respective centers essentially coincided with the points on the rotor disk with polar coordinates ($\dfrac{\bar{r}_0}{2}$, 0°) and

($\frac{\bar{r}_0}{2}$, 180°), respectively. Each vortex tube was assumed to have circumferentially uniform vortex strength, equal to $\bar{\gamma}_{1c}$ for the first tube and $-\bar{\gamma}_{1c}$ for the second one.

The same approach was employed for the lateral harmonic component of circulatory loading. Two new vortex tubes of radius $\frac{\bar{r}_0}{2}$ were assumed whose centers were positioned on the rotor disc at polar coordinates ($\frac{\bar{r}_0}{2}$, 90°) and ($\frac{\bar{r}_0}{2}$, 270°), in that order (Fig. 2). The vorticity strength of each vortex tube was set equal to $\bar{\gamma}_{1s}$ and $-\bar{\gamma}_{1s}$, in the first and second instances, respectively. Therefore, the original problem related to the first harmonic variations of rotor bound circulation was effectively reduced to a simpler one that was similar to the mean loading case. Equation (11) was then employed to estimate the inflow perturbations due to each of the centrally offset vortex tubes across the rotor disk. Using the principle of superposition, the inflow perturbations of the individual vortex tubes (Fig. 2) were mathematically summed and expressed as functions of the cyclic components of vorticity strength as follows:

$$\Delta u^{cyc}(\bar{r},\psi) = -\left\{\begin{array}{ll} \frac{\bar{\gamma}_{1c}}{2}[\kappa_c X \bar{r}_0 d_1(\hat{r})\cos\psi + \kappa_s X \bar{r}_0 d_2(\hat{r})\sin\psi] + & \\ \frac{\bar{\gamma}_{1s}}{2}[\kappa_c X \bar{r}_0 d_4(\hat{r})\sin\psi] + & \\ \frac{\bar{\gamma}_{1s}}{2}[\kappa_s X \bar{r}_0 d_2(\hat{r})\cos\psi] + & (\hat{r}<1) \\ & \\ \frac{\bar{\gamma}_{1c}}{2}[\kappa_c X \bar{r}_0 d_3(\hat{r})\cos\psi + \kappa_s X \bar{r}_0 d_2(\hat{r})\sin\psi] + & \\ \frac{\bar{\gamma}_{1s}}{2}[\kappa_c X \bar{r}_0 d_5(\hat{r})\sin\psi] + & \\ \frac{\bar{\gamma}_{1s}}{2}[\kappa_s X \bar{r}_0 d_2(\hat{r})\cos\psi] + & (\hat{r}>1) \end{array}\right\} \tag{12}$$

The superscript $()^{cyc}$ in Eq. (12) denotes that the specific perturbations are due to the cyclic components of circulatory loading, The symbols $d_i(\hat{r}),\ i = 1, 2, ...5$ are geometric influence coefficients (Ref. 18).

The total inflow perturbations across the rotor disk $\Delta u(\bar{r},\psi)$ that are induced by the configuration of a single set of vortex tubes such as the one described above (Fig. 2), can be obtained by summing the contribution of the flow components associated with the mean and cyclic variations of disk loading:

$$\Delta u(\bar{r},\psi) = \Delta u^{mean}(\bar{r},\psi) + \Delta u^{cyc}(\bar{r},\psi) \tag{13}$$

It is noted that, similarly to the individual Eqs. (11, 12), Eq. (13) implicitly consists of two specific parts; (a) a part that denotes the influence of the prescribed vortex tube set on the disk area enclosed by the tube of radius r_0 ($\hat{r}<1$) and (b) a part that essentially reflects the effect outside this region ($\hat{r}>1$).

Generalized vortex tube model

The preceding vortex tube analysis is applicable under the premise of constant bound circulation along the rotor disk radial coordinate. However, this is a rather crude approximation of the actual variation of aerodynamic loading that a helicopter rotor blade may encounter in flight. Therefore, the baseline vortex tube analysis of Ref. 18 is now extended to account for the effects of an arbitrary radial distribution of circulatory loading. Expressing the mean ($\bar{\Gamma}_0$) and first harmonic azimuthal components ($\bar{\Gamma}_{1c}$, $\bar{\Gamma}_{1s}$) of rotor bound circulation used in the RHS of Eq. (7), as linear superpositions of normalized associated Legendre function of the first kind $\bar{P}_n^m(\nu)$, essentially leads to the following expressions:

$$\bar{\Gamma}_0(\bar{r}) = \sum_{n=1,\ 3,\ 5\ldots}^{\infty} \tau_n^0 \bar{P}_n^0(\nu) \quad (14) \qquad \bar{\Gamma}_{1c}(\bar{r}) = \sum_{n=2,\ 4,\ 6\ldots}^{\infty} \tau_n^{1c} \bar{P}_n^1(\nu) \quad (15) \qquad \bar{\Gamma}_{1s}(\bar{r}) = \sum_{n=2,\ 4,\ 6\ldots}^{\infty} \tau_n^{1s} \bar{P}_n^1(\nu) \quad (16)$$

The radial expansion of disk bound circulation using normalized Legendre functions (Eqs. (14–16)) is carried out in accordance with the mathematical description of induced flow that is adapted in the original model of Peters and He (Eq. (1)). This approach is employed to maintain consistency between the two theories and enables the derivation of the associated wake curvature perturbation coefficients in integral form. The symbols τ_n^0, τ_n^{1c}, and τ_n^{1s} denote the generalized pressure force coefficients corresponding to the mean (τ_n^0) and first harmonic (τ_n^{1c}, τ_n^{1s}) components of circulatory disk loading. These are time-dependent, user-supplied integrals that depend only on the radial distribution of rotor bound circulation. As such, they are uniquely determined by the aerodynamic theory that is used to estimate the circulatory blade lift.

Using the associated Legendre functions for the radial expansion of rotor bound circulation (Eqs. (14–16)), the overall distribution of circulatory loading across the rotor disk can now be expressed up to the first harmonic component of aerodynamic pressure as shown below:

$$\bar{\Gamma}(\bar{r}, \psi) = \bar{\Gamma}_0(\bar{r}) + \bar{\Gamma}_{1c}(\bar{r}) \cos\psi + \bar{\Gamma}_{1s}(\bar{r}) \sin\psi \quad (17)$$

The unsteady wake that is generated due to the generalized pressure forces on a rotor disk of normalized radius equal to unity ($\bar{r} \in (0, 1)$) is now also expressed as a linear superposition of an infinite series of concentric, differential vortex tube configurations of radius $\bar{r}_0 \in (0, 1)$, such as the one illustrated in Fig. 2.

According to lifting line theory (Ref. 20), a radial step change in blade bound circulation $\frac{\partial\bar{\Gamma}(\bar{r},\psi)}{\partial\bar{r}}d\bar{r}$, results in the shedding of a trailed vortex element of azimuthal orientation and equal circulation. In a manner similar to the baseline vortex tube model of Ref. 18, the generalized formulation of this work assumes that the trailed vortex elements generated at a radial location $\bar{r}_0 \in (0,1)$, are wrapped around a continuous surface of vorticity. This surface corresponds to the outer boundary of the assumed differential vortex tube configuration or radius $\bar{r}_0$ (Fig. 2). Hence, according to Eqs. (8–10), the mean ($d\bar{\gamma}_0$) and first harmonic ($d\bar{\gamma}_{1c}$ and $d\bar{\gamma}_{1s}$) differential components of vortity strength with respect to a vortex tube configuration of radius $\bar{r}_0$, can be related to the radial distribution of rotor bound circulation as follows:

$$d\bar{\gamma}_0(\bar{r}_0) = \frac{1}{V_T}\sum_{n=1,\ 3,\ 5,\ldots}^{\infty}\tau_n^0\left(\frac{\partial\bar{P}_n^0(\nu_0)}{\partial\bar{r}}\right)\mathrm{d}\bar{r}_0 \tag{18a}$$

$$d\bar{\gamma}_{1c}(\bar{r}_0) = \frac{1}{V_T}\sum_{n=2,\ 4,\ 6,\ldots}^{\infty}\tau_n^{1c}\left(\frac{\partial\bar{P}_n^1(\nu_0)}{\partial\bar{r}}\right)\mathrm{d}\bar{r}_0 \tag{18b}$$

$$d\bar{\gamma}_{1s}(\bar{r}_0) = \frac{1}{V_T}\sum_{n=2,\ 4,\ 6,\ldots}^{\infty}\tau_n^{1s}\left(\frac{\partial\bar{P}_n^1(\nu_0)}{\partial\bar{r}}\right)\mathrm{d}\bar{r}_0 \tag{18c}$$

with $\nu_0 = \sqrt{1-\bar{r}_0^2}$, which indicates that the derivatives of the Legendre functions $P_n^m(\nu)$ are evaluated at $\bar{r} = \bar{r}_0$. Equation (13) can then be utilized to evaluate the inflow perturbations across the rotor disc due to a differential vortex tube configuration of radius $\bar{r}_0$ and strength components $d\bar{\gamma}_0$, $d\bar{\gamma}_{1c}$, and $d\bar{\gamma}_{1s}$.

It can be observed by inspecting Eqs. (18a–18c) that the mean and first harmonic differential components of vorticity strength are linear functions of $\frac{\partial\bar{P}_n^m(\nu)}{\partial\bar{r}} = \frac{d\bar{P}_n^m(\nu)}{d\bar{r}}$; the first derivatives of the associated Legendre functions with respect to the non-dimensional radial coordinate $\bar{r}$. Reference 9 noted that $\frac{\bar{P}_n^m(\nu)}{\nu} = \phi_n^m(\bar{r})$, where the parameter $\phi_n^m(\bar{r})$ was expressed in analytical closed form as written below:

$$\phi_n^m(\bar{r}) = \sqrt{(2n+1)H_n^m}\sum_{q=m,\ m+2,\ldots}^{n-1}\bar{r}^q(-1)^{(q-m)/2}\frac{(n+q)!\,!}{(q-m)!\,!\,(q+m)!\,!\,(n-q-1)!\,!} \tag{19}$$

with $H_n^m = \frac{(n+m-1)!\,!\,(n-m-1)!\,!}{(n+m)!\,!\,(n-m)!\,!}$. Hence, it is follows that since $\frac{d\bar{P}_n^m(\nu)}{d\bar{r}}$ is a sole function of $\bar{r}$, it can also be derived in closed form. This process essentially leads to the following expression:

$$\frac{d\bar{P}_n^m(\nu)}{d\bar{r}} = \frac{d\phi_n^m(\bar{r})}{d\bar{r}}\sqrt{1-\bar{r}^2} - \frac{\phi_n^m(\bar{r})}{\sqrt{1-\bar{r}^2}}\bar{r} \tag{20}$$

where $\frac{d\phi_n^m(\bar{r})}{d\bar{r}}$ can easily be derived in closed form by differentiating Eq. (19) in an analytical manner.

The total inflow perturbations $\Delta\lambda(\bar{r},\psi)$ induced by the whole distorted wake across the rotor disk, can be calculated by integrating radially the individual flow components induced by each differential vortex tube configuration of radius $\bar{r}_0 \in (0,1)$. This process can be mathematically expressed as follows:

$$\Delta\lambda(\bar{r},\psi) = \int_{\bar{r}_0=0}^{\bar{r}_0=1} \mathrm{d}u(\bar{r},\psi)_{\bar{r}_0} \tag{21}$$

where essentially $\mathrm{d}u(\bar{r},\psi)_{\bar{r}_0} = \Delta u(\bar{r},\psi)$ (Eq. (13)) when setting $\bar{\gamma}_0 = d\bar{\gamma}_0(\bar{r}_0)$, $\bar{\gamma}_{1c} = d\bar{\gamma}_{1c}(\bar{r}_0)$, and $\bar{\gamma}_{1s} = d\bar{\gamma}_{1s}(\bar{r}_0)$ as defined by Eqs. (18a–18c). Due to the fact that different expressions apply in the RHS of Eq. (13) for the evaluation of $\Delta u(\bar{r},\psi)$ depending on the value of the ratio $\hat{r} = \dfrac{\bar{r}}{\bar{r}_0}$, it is necessary to split the integral located in the RHS of Eq. (21) in two separate parts. This is written below for clarity:

$$\Delta\lambda(\bar{r},\psi) = \left(\int_{\bar{r}_0=0}^{\bar{r}_0\simeq\bar{r}} \mathrm{d}u(\bar{r},\psi)_{\bar{r}_0}\right)_{\hat{r}<1} + \left(\int_{\bar{r}_0\simeq\bar{r}}^{\bar{r}_0=1} \mathrm{d}u(\bar{r},\psi)_{\bar{r}_0}\right)_{\hat{r}>1} \tag{22}$$

where the subscripts $()_{\hat{r}<1}$ and $()_{\hat{r}>1}$ in the RHS of Eq. (22) denote the corresponding domains for which the reciprocal parts of Eq. (13) can be used for the mathematical evaluation of $\mathrm{d}u(\bar{r},\psi)_{\bar{r}_0}$. It is noted that due to the singular nature of the Biot–Savart law when $\bar{r}_0 = \bar{r}$, Eq. (13) results in infinite induced velocities at the vortex tube boundaries ($\hat{r} = 1$). Therefore, in order to de-singularize the problem at hand, the respective upper and lower limits of the definite integrals in the RHS of Eq. (22) are set asymptotically equal to $\bar{r}$ so that it always applies that $\hat{r} \neq 1$.

Combining Eqs. (11–13, 22) with Eqs. (18a–18c), after a series of extensive mathematical manipulations which are omitted for brevity, results in the following expression for the perturbed rotor inflow:

$$\Delta\lambda(\bar{r},\psi) = -\frac{1}{2V_T}\left\{\begin{array}{l} \kappa_c\left[\displaystyle\sum_{n=1,\,3\ldots}^{\infty} \tau_n^0 a_n(\bar{r})\cos\psi\right] + \kappa_s\left[\displaystyle\sum_{n=1,\,3\ldots}^{\infty} \tau_n^0 b_n(\bar{r})\sin\psi\right] + \\ \kappa_c X\left[\displaystyle\sum_{n=1,\,3\ldots}^{\infty} \tau_n^0\left(c_n^1(\bar{r}) + c_n^2(\bar{r})\cos 2\psi\right) + \sum_{n=2,\,4\ldots}^{\infty}\left(\tau_n^{1c} c_n^3(\bar{r})\cos\psi + \tau_n^{1s} c_n^4(\bar{r})\sin\psi\right)\right] + \\ \kappa_s X\left[\displaystyle\sum_{n=1,\,3\ldots}^{\infty} \tau_n^0 d_n^1(\bar{r})\sin 2\psi + \sum_{n=2,\,4\ldots}^{\infty}\left(\tau_n^{1c} d_n^2(\bar{r})\sin\psi + \tau_n^{1s} d_n^3(\bar{r})\cos\psi\right)\right] + \\ \kappa_c X^2\left[\displaystyle\sum_{n=1,\,3\ldots}^{\infty} \tau_n^0 \frac{3}{2}\left(e_n^1(\bar{r})\cos\psi + e_n^2(\bar{r})\cos 3\psi\right)\right] + \\ \kappa_s X^2\left[\displaystyle\sum_{n=1,\,3\ldots}^{\infty} \tau_n^0 \frac{3}{2}\left(f_n^1(\bar{r})\sin\psi + f_n^2(\bar{r})\sin 3\psi\right)\right] \end{array}\right\} \tag{23}$$

where the radial functions in Eq. (23) are essentially geometric influence coefficients that are given by the

following integral expressions:

$$a_n(\bar{r}) = b_n(\bar{r}) = \bar{r}\int_0^{\bar{r}} \left(\frac{d\bar{P}_n^0(\nu_0)}{d\bar{r}}\right) \mathrm{d}\bar{\mathrm{r}}_0 \tag{24a}$$

$$c_n^1(\bar{r}) = \int_0^{\bar{r}} \left(\frac{d\bar{P}_n^0(\nu_0)}{d\bar{r}}\right) \bar{r}_0 e_1(\hat{r}) \mathrm{d}\bar{\mathrm{r}}_0 + \int_{\bar{r}}^1 \left(\frac{d\bar{P}_n^0(\nu_0)}{d\bar{r}}\right) \bar{r}_0 e_3(\hat{r}) \mathrm{d}\bar{\mathrm{r}}_0 \tag{24b}$$

$$c_n^2(\bar{r}) = d_n^1(\bar{r}) = \int_0^{\bar{r}} \left(\frac{d\bar{P}_n^0(\nu_0)}{d\bar{r}}\right) \bar{r}_0 e_2(\hat{r}) \mathrm{d}\bar{\mathrm{r}}_0 + \int_{\bar{r}}^1 \left(\frac{d\bar{P}_n^0(\nu_0)}{d\bar{r}}\right) \bar{r}_0 e_4(\hat{r}) \mathrm{d}\bar{\mathrm{r}}_0 \tag{24c}$$

$$c_n^3(\bar{r}) = \int_0^{\bar{r}} \left(\frac{d\bar{P}_n^1(\nu_0)}{d\bar{r}}\right) \bar{r}_0 d_1(\hat{r}) \mathrm{d}\bar{\mathrm{r}}_0 + \int_{\bar{r}}^1 \left(\frac{d\bar{P}_n^1(\nu_0)}{d\bar{r}}\right) \bar{r}_0 d_3(\hat{r}) \mathrm{d}\bar{\mathrm{r}}_0 \tag{24d}$$

$$c_n^4(\bar{r}) = \int_0^{\bar{r}} \left(\frac{d\bar{P}_n^1(\nu_0)}{d\bar{r}}\right) \bar{r}_0 d_4(\hat{r}) \mathrm{d}\bar{\mathrm{r}}_0 + \int_{\bar{r}}^1 \left(\frac{d\bar{P}_n^1(\nu_0)}{d\bar{r}}\right) \bar{r}_0 d_5(\hat{r}) \mathrm{d}\bar{\mathrm{r}}_0 \tag{24e}$$

$$d_n^2(\bar{r}) = d_n^3(\bar{r}) = \int_0^1 \left(\frac{d\bar{P}_n^1(\nu_0)}{d\bar{r}}\right) \bar{r}_0 d_2(\hat{r}) \mathrm{d}\bar{\mathrm{r}}_0 \tag{24f}$$

$$e_n^1(\bar{r}) = -f_n^1(\bar{r}) = -\bar{r}\int_0^{\bar{r}} \left(\frac{d\bar{P}_n^0(\nu_0)}{d\bar{r}}\right) \mathrm{d}\bar{\mathrm{r}}_0 + \int_{\bar{r}}^1 \left(\frac{d\bar{P}_n^0(\nu_0)}{d\bar{r}}\right) \bar{r}_0 e_5(\hat{r}) \mathrm{d}\bar{\mathrm{r}}_0 \tag{24g}$$

$$e_n^2(\bar{r}) = f_n^2(\bar{r}) = \int_{\bar{r}}^1 \left(\frac{d\bar{P}_n^0(\nu_0)}{d\bar{r}}\right) \bar{r}_0 e_6(\hat{r}) \mathrm{d}\bar{\mathrm{r}}_0 \tag{24h}$$

Equation (23) along with Eqs. (24a–24h) constitute a generalized vortex tube tube model applicable to any radial distribution of rotor bound circulation. The developed approach can be used to evaluate the flow perturbations due to the influence of wake curvature, along with the aerodynamic coupling between wake curvature (k_c, k_s) and skew X. The model is compatible with any induced flow theory that employs associated Legendre functions $\bar{P}_n^m(\nu)$ to express the radial distribution of pressure on the rotor disk.

Inflow perturbation coefficients for finite-state induced flow models

This section aims to deploy the developed generalized vortex tube approach (Eq. (23)) in order to augment the induced flow model of Peters and He (Eqs. (2a, 2b)) to account for the effect of rotor wake curvature in hover and forward flight, along with the coupling between wake curvature and wake skew. The goal is to derive a finite series of inflow perturbation coefficients that can be linearly superimposed on the existing inflow gain matrices of the Peters–He model, similarly to the Krothapalli model (Eq. (3)).

Equation (1) provides the normalized distribution of induced flow across the rotor disk as expressed in the formulation of Peters and He. A perturbation in the distribution of inflow can be expressed as follows:

$$\Delta\lambda(\bar{r},\psi) = \sum_{r=0}^{\infty} \sum_{j=r+1,\ r+3,\ldots}^{\infty} \phi_j^r(\bar{r})[\Delta\alpha_j^r \cos r\psi + \Delta\beta_j^r \sin r\psi] \tag{25}$$

The inflow perturbation coefficients ($\Delta\alpha_j^r$ and $\Delta\beta_j^r$) can be obtained by invoking the orthogonality condi-

tions with respect to the employed trigonometric functions and associated Legendre polynomials (Ref. 18):

$$\Delta\alpha_j^0 = \frac{1}{2\pi}\int_0^1 \left[\int_0^{2\pi} \Delta\lambda(\bar{r},\psi)\mathrm{d}\psi\right] \bar{P}_j^0(\nu)\,\bar{r}\,\mathrm{d}\bar{\mathrm{r}}, \qquad r=0,\ j=r+1,r+3,\ldots \tag{26a}$$

$$\Delta\alpha_j^r = \frac{1}{\pi}\int_0^1 \left[\int_0^{2\pi} \Delta\lambda(\bar{r},\psi)\cos r\psi\,\mathrm{d}\psi\right] \bar{P}_j^r(\nu)\,\bar{r}\,\mathrm{d}\bar{\mathrm{r}}, \qquad r\geq 1,\ j=r+1,r+3,\ldots \tag{26b}$$

$$\Delta\beta_j^r = \frac{1}{\pi}\int_0^1 \left[\int_0^{2\pi} \Delta\lambda(\bar{r},\psi)\sin r\psi\,\mathrm{d}\psi\right] \bar{P}_j^r(\nu)\,\bar{r}\,\mathrm{d}\bar{\mathrm{r}}, \qquad r\geq 1,\ j=r+1,r+3,\ldots \tag{26c}$$

where $\Delta\lambda(\bar{r},\psi)$ can be evaluated using Eq. (23). The integrals $\left[\int_0^{2\pi}(\ldots)\,\mathrm{d}\psi\right]$ in the RHS of Eqs. (26a–26c) can be obtained in closed form as functions of the geometric influence coefficients (Eqs. (24a–24h)). Subsequently, the required perturbation coefficients ($\Delta\alpha_j^r$, $\Delta\beta_j^r$) can be evaluated analytically using Eqs. (26a–26c). After a series of mathematical manipulations the following expressions are derived:

$$\Delta\alpha_j^0 = \qquad -\frac{1}{2V_T}\left\{\kappa_c X\left[\sum_{n=1,\,3\ldots}^{\infty}\tau_n^0\left(\int_0^1 c_n^1(\bar{r})\bar{P}_j^0(\nu)\bar{r}\,\mathrm{d}\bar{r}\right)\right]\right\} \tag{27}$$

$$\Delta\alpha_j^r = -\frac{1}{2V_T}\left\{\begin{array}{ll} \kappa_c\left[\displaystyle\sum_{n=1,\,3\ldots}^{\infty}\tau_n^0\left(\int_0^1 a_n(\bar{r})\bar{P}_j^1(\nu)\bar{r}\,\mathrm{d}\bar{r}\right)\right] + \kappa_c X\left[\displaystyle\sum_{n=2,\,4\ldots}^{\infty}\tau_n^{1c}\left(\int_0^1 c_n^3(\bar{r})\bar{P}_j^1(\nu)\bar{r}\,\mathrm{d}\bar{r}\right)\right] + & \\ \kappa_s X\left[\displaystyle\sum_{n=2,\,4\ldots}^{\infty}\tau_n^{1s}\left(\int_0^1 d_n^3(\bar{r})\bar{P}_j^1(\nu)\bar{r}\,\mathrm{d}\bar{r}\right)\right] + \kappa_c X^2\left[\frac{3}{2}\displaystyle\sum_{n=1,\,3\ldots}^{\infty}\tau_n^0\left(\int_0^1 e_n^1(\bar{r})\bar{P}_j^1(\nu)\bar{r}\,\mathrm{d}\bar{r}\right)\right], & (r=1) \\ \kappa_c X\left[\displaystyle\sum_{n=1,\,3\ldots}^{\infty}\tau_n^0\left(\int_0^1 c_n^2(\bar{r})\bar{P}_j^2(\nu)\bar{r}\,\mathrm{d}\bar{r}\right)\right], & (r=2) \\ \kappa_c X^2\left[\frac{3}{2}\displaystyle\sum_{n=1,\,3\ldots}^{\infty}\tau_n^0\left(\int_0^1 e_n^2(\bar{r})\bar{P}_j^3(\nu)\bar{r}\,\mathrm{d}\bar{r}\right)\right], & (r=3) \end{array}\right\} \tag{28}$$

$$\Delta\beta_j^r = -\frac{1}{2V_T}\left\{\begin{array}{ll} \kappa_s\left[\displaystyle\sum_{n=1,\,3\ldots}^{\infty}\tau_n^0\left(\int_0^1 b_n(\bar{r})\bar{P}_j^1(\nu)\bar{r}\,\mathrm{d}\bar{r}\right)\right] + \kappa_c X\left[\displaystyle\sum_{n=2,\,4\ldots}^{\infty}\tau_n^{1s}\left(\int_0^1 c_n^4(\bar{r})\bar{P}_j^1(\nu)\bar{r}\,\mathrm{d}\bar{r}\right)\right] + & \\ \kappa_s X\left[\displaystyle\sum_{n=2,\,4\ldots}^{\infty}\tau_n^{1c}\left(\int_0^1 d_n^2(\bar{r})\bar{P}_j^1(\nu)\bar{r}\,\mathrm{d}\bar{r}\right)\right] + \kappa_s X^2\left[\frac{3}{2}\displaystyle\sum_{n=1,\,3\ldots}^{\infty}\tau_n^0\left(\int_0^1 f_n^1(\bar{r})\bar{P}_j^1(\nu)\bar{r}\,\mathrm{d}\bar{r}\right)\right], & (r=1) \\ \kappa_s X\left[\displaystyle\sum_{n=1,\,3\ldots}^{\infty}\tau_n^0\left(\int_0^1 d_n^1(\bar{r})\bar{P}_j^2(\nu)\bar{r}\,\mathrm{d}\bar{r}\right)\right], & (r=2) \\ \kappa_s X^2\left[\frac{3}{2}\displaystyle\sum_{n=1,\,3\ldots}^{\infty}\tau_n^0\left(\int_0^1 f_n^2(\bar{r})\bar{P}_j^3(\nu)\bar{r}\,\mathrm{d}\bar{r}\right)\right], & (r=3) \end{array}\right\} \tag{29}$$

Equations (27–29) relate the j^{th} Legendre polynomial of the r^{th} harmonic of induced flow due to the effect of wake curvature (k_c, k_s), to the n^{th} polynomial of the zeroth (τ_n^0) and first harmonic (τ_n^{1c}, τ_n^{1s}) components of aerodynamic pressure on the rotor disk. It can be observed that the induced flow perturbations expressed by Eqs. (27–29) comprise periodic terms with frequency content that reaches up to the third harmonic of inflow ($r = 3$). Any higher-frequency periodic terms ($r \geq 4$) are not accounted for by the present approach. This is because the baseline vortex tube analysis of Ref. 18 (Eqs. (11, 12)), upon which the generalized vortex tube model of this paper has been formulated (Eq. (23)), caters only for trigonometric terms that reach up to third harmonic component of azimuth angle ψ on the rotor disk.

Equations (27–29) can be expressed in a partitioned matrix form as written below:

$$\begin{Bmatrix} \Delta\alpha_j^r \\ \Delta\beta_j^r \end{Bmatrix} = -\frac{1}{2V_T}\left[[D]_0 + [D]_1 X + [D]_2 X^2\right]\begin{Bmatrix} \tau_n^{mc} \\ \tau_n^{ms} \end{Bmatrix} \tag{30}$$

The matrices $[D]_0$, $[D]_1$, and $[D]_2$ in Eq. (30) contain the inflow coupling coefficients due to the influence of wake curvature ($[D]_0$), along with the linear ($[D]_1$) and quadratic ($[D]_2$) coupling effects between wake curvature and skew X. These matrices can be decompositioned in partitioned matrix form as follows:

$$[D]_0 = \kappa_c \begin{bmatrix} \left[C_{j,n}^{r,m}\right]_c^{cc} & \left[C_{j,n}^{r,m}\right]_c^{cs} \\ \left[C_{j,n}^{r,m}\right]_c^{sc} & \left[C_{j,n}^{r,m}\right]_c^{ss} \end{bmatrix} + \kappa_s \begin{bmatrix} \left[C_{j,n}^{r,m}\right]_s^{cc} & \left[C_{j,n}^{r,m}\right]_s^{cs} \\ \left[C_{j,n}^{r,m}\right]_s^{sc} & \left[C_{j,n}^{r,m}\right]_s^{ss} \end{bmatrix} \tag{31a}$$

$$[D]_1 = \kappa_c \begin{bmatrix} \left[C_{j,n}^{r,m}\right]_{cX}^{cc} & \left[C_{j,n}^{r,m}\right]_{cX}^{cs} \\ \left[C_{j,n}^{r,m}\right]_{cX}^{sc} & \left[C_{j,n}^{r,m}\right]_{cX}^{ss} \end{bmatrix} + \kappa_s \begin{bmatrix} \left[C_{j,n}^{r,m}\right]_{sX}^{cc} & \left[C_{j,n}^{r,m}\right]_{sX}^{cs} \\ \left[C_{j,n}^{r,m}\right]_{sX}^{sc} & \left[C_{j,n}^{r,m}\right]_{sX}^{ss} \end{bmatrix} \tag{31b}$$

$$[D]_2 = \kappa_c \begin{bmatrix} \left[C_{j,n}^{r,m}\right]_{cX^2}^{cc} & \left[C_{j,n}^{r,m}\right]_{cX^2}^{cs} \\ \left[C_{j,n}^{r,m}\right]_{cX^2}^{sc} & \left[C_{j,n}^{r,m}\right]_{cX^2}^{ss} \end{bmatrix} + \kappa_s \begin{bmatrix} \left[C_{j,n}^{r,m}\right]_{sX^2}^{cc} & \left[C_{j,n}^{r,m}\right]_{sX^2}^{cs} \\ \left[C_{j,n}^{r,m}\right]_{sX^2}^{sc} & \left[C_{j,n}^{r,m}\right]_{sX^2}^{ss} \end{bmatrix} \tag{31c}$$

where the subscripts $()_c$, $()_s$ signify that the corresponding $[C]$ partitions contain influence coefficients associated with the effect of longitudinal (κ_c) and lateral (κ_s) wake curvature, respectively. Similarly, the subscripts $()_{cX}$, $()_{sX}$ and $()_{cX^2}$, $()_{sX^2}$ indicate that the associated $[C]$ partitions represent the coupling between wake curvature and skew in a linear ($\kappa_c X$, $\kappa_s X$) and quadratic ($\kappa_c X^2$, $\kappa_s X^2$) manner, respectively.

The $[C_{n,j}^{r,m}]$ matrices in Eqs. (31a–31c) are partitioned so that the superscripts r, m are row-column indices of a specific partition, whilst the subscripts j, n are element indices within each partition. In order to maintain consistency with the finite-state inflow model of Peters and He (Ref. 9), it applies that r, m

$= 0, 1, 2, 3 \ldots$ for the cosine terms and $r, m = 1, 2, 3 \ldots$ for the sine terms. Furthermore, the indices j, n do not take consecutive integer values. Instead, it follows that $j = r+1, r+3 \ldots$ and $n = m+1, m+3 \ldots$. In addition, the superscripts $()^{cc,cs,sc,ss}$ signify that the corresponding partitioned matrices represent the aerodynamic coupling between the cosine $()^c$ and sine $()^s$ parts of Eq. (25). As an example, it is noted that the $[C_{n,j}^{r,m}]^{cs}$ matrix contains the influence coefficients that relate the j^{th} Legendre polynomial of the r^{th} cosinusoidal harmonic of inflow, to the n^{th} polynomial of the m^{th} sinusoidal harmonic of aerodynamic pressure, due to the effect of rotor wake curvature and the implicit coupling between curvature and skew.

The individual values of the perturbation coefficients within their respective partitions $[C_{j,n}^{r,m}]$ in the RHS of Eqs. (31a–31c), can be determined by equating the RHS of Eqs. (27–29) with the RHS of Eq. (30). This leads to the following expressions for the cosine-cosine (cc) inflow–pressure coupling coefficients:

$$[C_{j,n}^{0,0}]_{cX}^{cc} = \int_0^1 c_n^1(\bar{r})\bar{P}_j^0(\nu)\bar{r}\,\mathrm{d}\bar{r} \quad (32) \qquad [C_{j,n}^{1,0}]_{c}^{cc} = \int_0^1 a_n(\bar{r})\bar{P}_j^1(\nu)\bar{r}\,\mathrm{d}\bar{r} \quad (33) \qquad [C_{j,n}^{1,0}]_{cX^2}^{cc} = \frac{3}{2}\int_0^1 e_n^1(\bar{r})\bar{P}_j^1(\nu)\bar{r}\,\mathrm{d}\bar{r} \quad (34)$$

$$[C_{j,n}^{1,1}]_{cX}^{cc} = \int_0^1 c_n^3(\bar{r})\bar{P}_j^1(\nu)\bar{r}\,\mathrm{d}\bar{r} \quad (35) \qquad [C_{j,n}^{2,0}]_{cX}^{cc} = \int_0^1 c_n^2(\bar{r})\bar{P}_j^2(\nu)\bar{r}\,\mathrm{d}\bar{r} \quad (36) \qquad [C_{j,n}^{3,0}]_{cX^2}^{cc} = \frac{3}{2}\int_0^1 e_n^2(\bar{r})\bar{P}_j^3(\nu)\bar{r}\,\mathrm{d}\bar{r} \quad (37)$$

and for the cosine-sine (cs) coupling coefficients:

$$[C_{j,n}^{1,1}]_{sX}^{cs} = \int_0^1 d_n^3(\bar{r})\bar{P}_j^1(\nu)\bar{r}\,\mathrm{d}\bar{r} \quad (38)$$

Similarly, for the sine-cosine (sc) inflow–pressure coupling perturbation coefficients, Eqs. (27–29) give:

$$[C_{j,n}^{1,0}]_{s}^{sc} = \int_0^1 b_n(\bar{r})\bar{P}_j^1(\nu)\bar{r}\,\mathrm{d}\bar{r} \quad (39) \qquad [C_{j,n}^{1,0}]_{sX^2}^{sc} = \frac{3}{2}\int_0^1 f_n^1(\bar{r})\bar{P}_j^1(\nu)\bar{r} \quad (40) \qquad [C_{j,n}^{1,1}]_{sX}^{sc} = \int_0^1 d_n^2(\bar{r})\bar{P}_j^1(\nu)\bar{r}\,\mathrm{d}\bar{r} \quad (41)$$

$$[C_{j,n}^{2,0}]_{sX}^{sc} = \int_0^1 d_n^1(\bar{r})\bar{P}_j^2(\nu)\bar{r}\,\mathrm{d}\bar{r} \quad (42) \qquad [C_{j,n}^{3,0}]_{sX^2}^{sc} = \frac{3}{2}\int_0^1 f_n^2(\bar{r})\bar{P}_j^3(\nu)\bar{r}\,\mathrm{d}\bar{r} \quad (43)$$

and finally, for sine-sine (ss) inflow-pressure coupling effects, it applies that:

$$[C_{j,n}^{1,1}]_{cX}^{ss} = \int_0^1 c_n^4(\bar{r})\bar{P}_j^1(\nu)\bar{r}\,\mathrm{d}\bar{r} \quad (44)$$

with all remaining values of $[C_{j,n}^{r,m}]$ not addressed by Eqs. (32–44) being effectively equal to zero. The inflow perturbation coefficients described by Eqs. (32–44) do not yet have closed form solutions. There-

fore, they have to be determined by evaluating the associated integrals numerically. The computed inflow perturbation coefficients can be saved into a database that can be loaded instantly prior to a simulation.

Similarly to the methodology followed by Krothapalli *et al.* in Ref. 15, the original finite-state inflow model of Peters and He (Eqs. (2a, 2b)) is now mathematically augmented to account for the effects of wake curvature in hover and forward flight, using the mathematical approach proposed in this paper. This is carried out by superimposing the newly-derived coefficients (Eqs. (31a–31c)) on the existing inflow gain matrices ($[L^c]$ and $[L^s]$) using the coupled inflow form of the model given by Eq. (3). This gives:

$$\begin{bmatrix} [M^c] & [0] \\ [0] & [M^s] \end{bmatrix} \begin{Bmatrix} \dot{\alpha}_j^r \\ \dot{\beta}_j^r \end{Bmatrix} + \begin{bmatrix} [V^c] & [0] \\ [0] & [V^s] \end{bmatrix} \left\{ \begin{bmatrix} [L^c] & [0] \\ [0] & [L^s] \end{bmatrix} + K_{Re}\,[\Delta L] \right\}^{-1} \begin{Bmatrix} \alpha_j^r \\ \beta_j^r \end{Bmatrix} = \frac{1}{2} \begin{Bmatrix} \tau_n^{mc} \\ \tau_n^{ms} \end{Bmatrix} \tag{45a}$$

$$[\Delta L] = -\{[D]_0 + [D]_1 X + [D]_2 X^2\} \tag{45b}$$

where K_{Re} is the wake curvature parameter (Ref. 15) also used in Krothapalli's model (Eq. (3)). The theoretical value of K_{Re} predicted by momentum theory is 1.0 (Ref. 18). According to Ref. 17, when using the approach of Krothapalli, the value of K_{Re} required for satisfactory correlation with measured data can reach up to 3.8. However, this value is non-physically large and not theoretically justified.

Equations (45a, 45b) combined with Eqs. (31a–31c) and the dynamic wake distortion model of Zhao and Prasad (Eq. (6)), constitute an improved finite-state induced flow approach that accounts for the effect of wake curvature in hover and forward flight. The proposed model caters for the linear ($\kappa_c X$, $\kappa_s X$) and quadratic ($\kappa_c X^2$, $\kappa_s X^2$) effects due to the aerodynamic coupling between wake curvature and skew. Furthermore, the method accounts for the previously omitted circumferential variations of disk loading along with higher-frequency content reaching up to the third harmonic component of rotor inflow.

Nonlinear modeling of flexible rotor blades for helicopter flight dynamics

To evaluate the potential and identify the limitations of the aerodynamic model described in this paper, the developed approach has been coupled with the finite-state inflow model of Peters–He (Refs. 8, 9) and the dynamic wake distortion model of Zhao–Prasad (Ref. 17). The combined approach has been coupled with the aeroelastic rotor model presented in Ref. 21. The formulation of Ref. 21 has been developed by the author for the simulation of rotor blade flexibility in real-time flight dynamics applications, whilst employing sufficient modeling fidelity for simultaneous prediction of oscillatory blade loads.

A minimum potential energy approach based on Lagrangian kinematics is utilized to obtain the natural vibration characteristics of the main rotor blades for flapwise, chordwise, and torsional deformation (Ref. 22). The rotor blade is treated as a continuous rotating system of nonuniform structural properties. The employed formulation for rotor dynamics in combination with the augmented induced flow model described in this paper, have been coupled with the dynamic stall model of Leishman and Beddoes (Ref. 23) for unsteady, nonlinear, blade element aerodynamics. The dynamic response of the elastic blades is calculated using a fifth-order accurate numerical evaluation scheme of the convolution integral.

The aircraft fuselage is treated dynamically as a rigid body with six degrees of freedom using the inertial tensor and mass properties provided in Ref. 24. Experimentally derived look-up tables, also extracted from Ref. 24, are employed for the estimation of the aerodynamic loads generated by the fuselage as functions of incidence and side-slip angles. Additional sets of look-up tables are utilized for the prediction of the aerodynamic behavior of the empennage. Steady-state two-dimensional airfoil characteristics along with first-order dynamic inflow (Ref. 11) are used for the prediction of tail-rotor performance.

A globally convergent Newton–Raphson method is incorporated to obtain rotor trim for a designated set of flight conditions. The numerical scheme is used for the solution of Euler's nonlinear differential equations for rigid body kinematics applied to the aircraft fuselage (Ref. 24). The main and tail rotors are marched simultaneously in time using the initial condition of nonexistent circulatory wake. The time-marching process continues until a once-per-rev (1P) periodic condition is achieved with respect to the main rotor mean and first harmonic multi-blade coordinates of flap ($\beta_0,\ \beta_{1c},\ \beta_{1s}$) and lead-lag motion ($\zeta_0,\ \zeta_{1c}$, and ζ_{1s}). Having achieved periodicity in the rotor response, a finite series of rotations is carried out where the main rotor forces and moments are time-averaged to acquire mean values for trim.

Estimation of Stability and Control (S & C) derivatives is conducted by numerically perturbing the integrated model around an acquired trim condition. Extraction of perturbation forces and moments is carried out when 1P periodicity is achieved with respect to the main rotor flap/lag multi-blade coordinates. The corresponding S & C derivatives are subsequently calculated using second-order central finite-differences. Simulation of nonlinear control response is carried out after obtaining rotor trim by applying a pre-defined schedule of rotor control inputs. Fourth-order Runge-Kutta integration is employed to integrate Euler's differential equations for rigid body kinematics applied to the aircraft fuselage.

Results and Discussion

The developed mathematical approach is initially applied to assess the aerodynamic effect of wake curvature on the dynamic response of an articulated rotor with a flap frequency ratio ν_β equal to unity. Subsequently, the integrated model is deployed to investigate the influence of wake curvature on the predicted stability and control response of a hingeless rotor helicopter modeled after the MBB Bo 105.

Unless indicated otherwise, a total of eight inflow harmonics ($m, r \leq 8$) are deployed to capture the effect of higher harmonic loading on the rotor inflow response. The associated Legendre functions $\bar{P}_n^m(\nu)$ used reach up to the tenth power of non-dimensional rotor radius $\bar{r}$. This particular inflow model configuration results in a dynamic-wake representation of 62 flow-states. A total of six flap/lag/torsion (F/L/T) vibration modes are employed in the respective rotor dynamics model, unless stated otherwise. It is noted that the aeroelastic rotor model used in this work has been extensively validated by the author in terms of trim, stability, nonlinear control response, and oscillatory blade loads in Refs. 21, 22, 25.

Effect of wake curvature on the dynamic response characteristics of an articulated rotor system

This section aims to assess the aerodynamic effect of rotor wake curvature on the control response characteristics of an articulated rotor system. A dynamically neutral 4-bladed rotor configuration ($N_B = 4$) is defined to isolate the aerodynamic effects from the structural (inertial and elastic) factors that influence the dynamic rotor response. The blades are treated as rigid bodies with freely-articulated flap and cantilever lead-lag boundary conditions. The described rotor model has a solidity of $\sigma = 0.07$, a tip-speed of 218 m/sec, and a nominal thrust coefficient of $C_T = 0.005$.

The term "dynamically neutral" refers to the fact that the rotor has a flap frequency ratio ν_β equal to unity. This means that the first natural frequency of blade flapping is equal to the rotor speed Ω. Thus, the blades are forced at resonance when a 1P harmonic excitation is applied. This results in a phase lag in the rotor response of exactly 90° in the azimuthal direction. Consequently, for any aerodynamic forcing applied in a sinusoidal manner (θ_{1s}) the on-axis rotor response has a strictly cosinusoidal character (β_{1c}) and vice-versa. Therefore, any sinusoidal flapping (β_{1s}) effectively denotes the off-axis rotor response. This fundamental rotor dynamics attribute allows to isolate the aerodynamic effects on the rotor cross-coupling characteristics from any factors related to the structural dynamics of the rotor blades.

A numerical experiment is carried out for hovering-flight conditions ($\lambda_f = \mu = 0$) and zero hub-

angular motions ($\bar{p} = \bar{q} = 0$). The rotor is initially trimmed in terms of collective pitch angle θ_0 to produce a non-dimensional thrust coefficient of $C_T = 0.005$. A designated control input schedule is subsequently applied comprising a sinusoidal harmonic excitation in longitudinal cyclic θ_{1s}. The employed control schedule is shown in Fig. 3. No perturbation is applied in terms of lateral cyclic ($\theta_{1c} = 0$) or collective pitch angle (θ_0). The off-axis rotor response (β_{1s}) is shown in Fig. 4. Results are presented using different values for the wake curvature parameter K_{Re} (Eqs. (45a, 45b)) reaching up to 5. The computations carried out for $K_{Re} = 0$ neglect the effect of wake curvature. Results are presented using the present wake model in Fig. 4(a), whilst the Krothapalli model (Refs. 14, 15) is employed for the predictions shown in Fig. 4(b).

Since the simulation is carried out for quiescent free-stream conditions ($\lambda_f = \mu = 0$), the effective wake curvature stems exclusively from the rate of first harmonic flapping caused mainly by the on-axis rotor response (β_{1c} due to $\delta\theta_{1s}$). The resultant wake curvature $(\kappa_c)_{qs}(\bar{t}) = \dfrac{-\dot{\bar{\beta}}_{1c}(\bar{t})}{\lambda_m(\bar{t})}$ induces longitudinal inflow gradients on the rotor disk, forcing the blades at resonance (1P). The blades respond with a phase-lag of 90° azimuth-wise resulting in off-axis flapping β_{1s}. This effect is reduced when the on-axis flapping β_{1c} is stabilized and its rate is diminished. The effect of wake curvature then fades-off exponentially as described by Eq. (6) and the off-axis flapping β_{1s} continues uninfluenced by wake distortion effects.

It can be observed by evaluating Figs. 4(a) and (b) that the curvature of the rotor wake has a detrimental effect on the off-axis rotor response. This effect is amplified with increasing values of K_{Re}. Although results are presented for values of K_{Re} up to 5.0, any value larger than 2.0 is non-physical (Ref. 18). As expected, including the effect of wake curvature increases the amplitude of the off-axis flapping. The response phase angle is also affected. Closer inspection of Figs. 3 and 4 reveals that accounting for the curved wake effect increases the phase correlation between the applied control schedule (Fig. 3) and the predicted off-axis rotor response (Fig. 4). The off-axis response observed when the curved wake effect is neglected ($K_{Re} = 0$), is attributed to the azimuthal variation of blade incidence that is generated purely due to the kinematics of blade flapping (Ref. 26). This effect is also included for the cases that $K_{Re} \neq 0$.

Figure 4(c) presents the quantified percentage differences observed in off-axis flapping (β_{1s}) between the two wake curvature models. The models agree both in terms of amplitude as well as phase angle. This result is not surprising considering that the Krothapalli wake model was also derived using vortex tube

theory applied to the specific case of zero wake skew angle ($\chi = 0°$, $X = 0$). However, the Krothapalli model neglects any circumferential variations of disk loading. In contrast, these are thoroughly accounted for by the present modeling approach. This is the dominant cause for the differences observed between the two models. These discrepancies are of the order of $\pm 3 - 4\%$ and seem to be slightly influenced by K_{Re}. The dependency on K_{Re} is attributed to the relative magnitude of the wake curvature effects related to the mean ($\bar{\Gamma}_0(\bar{r})$) and first harmonic components ($\bar{\Gamma}_{1c}(\bar{r})$ and $\bar{\Gamma}_{1s}(\bar{r})$) of circulatory loading.

Thus, it can be concluded that the developed wake curvature model agrees very well with the existing approach of Krothapalli (Ref. 15) for hovering-flight conditions. The developed theory improves on the existing model by including the first harmonic azimuthal variations of circulatory disk loading ($\bar{\Gamma}_{1c}(\bar{r})$ and $\bar{\Gamma}_{1s}(\bar{r})$) that were previously omitted. Furthermore, the influence of K_{Re} on the predictions made with both models has been shown to be nearly identical for axial flow conditions. This indicates that both wake curvature models exhibit very similar physical behavior for the specific case of zero wake skew angle.

Effect of wake curvature on predicted stability characteristics

This section aims to evaluate the effect of wake curvature on the predicted stability derivatives of the Bo 105 helicopter. Analysis has been carried out for straight and level flight at $V \approx 41.15\ m/sec$ corresponding to an advance ratio of $\mu \approx 0.189$. The quasi-steady wake skew angle χ is roughly 82°. Reference 27 reported on system identification methods for the extraction of S & C derivatives from flight test data. Results were obtained from various working group members that include; the U.S Army Aeroflightdynamics Directorate (AFDD), the German aerospace center DLR (Deutsches Zentrum für Luft– und Raumfahrt), and the Canadian National Aeronautical Establishment (NAE).

Tables 1 and 2 present correlations for the pitch–roll damping (M_q and L_p) and off-axis cross-coupling stability derivatives (M_p and L_q) of the Bo 105 helicopter. Comparisons are carried out between numerical predictions and system identification results reported by AFDD, DLR, and NAE in Ref. 27. Computational results obtained using the present wake curvature model and the approach of Krothapalli (Ref. 15) are presented in Tables 1 and 2, respectively. The associated standard deviations (σ) of the derivatives identified from flight test data are also provided in parentheses. These represent the theoretically lowest achievable standard deviation for each identified derivative (Cramẽr–Rao lower bounds).

It can be readily observed from the results presented in Tables 1 and 2 that there are significant differ-

ences between the identified values considering the derivatives of interest. Fairly accurate prediction of both pitch–roll damping (M_q and L_p) and cross-coupling derivative groups (M_p and L_q) can be observed in Table 1 when using the present wake modeling approach with $K_{Re} \geq 1.0$. As expected, the effect of wake curvature is significantly more apparent on the pitch and roll cross-coupling derivatives, compared to the influence noted on the respective damping derivatives. The influence observed on the damping derivatives is attributed to the well-known cross-coupling characteristics of the Bo 105 helicopter (Ref. 27).

The pitch and roll damping derivatives, M_q and L_p respectively, are influenced predominantly by inertial loads related to the gyroscopic precession of the blades as well as by the in-plane aerodynamic loads (Ref. 26). These components are thoroughly accounted for in the present modeling approach through inclusion of the respective forcing terms in the employed equations of motion (Ref. 21). It can be observed in Table 1 that when using a nominal value for $K_{Re} = 1.0$, the developed approach yields damping derivatives that are in good agreement with those identified by the various working group members.

When using the present modeling approach with $K_{Re} = 2.0$, the effect of wake curvature reduces the predicted absolute values of M_q and L_p by approximately 4% and 28%, respectively, relative to the case when the influence of a curved wake is neglected ($K_{Re} = 0$). As expected, for cruising flight conditions the effect of wake curvature on pitch damping M_q is significantly lower compared to its influence on the roll damping derivative L_p. This is attributed to the quasi-steady longitudinal wake-skew angle χ which reaches roughly 82° for the imposed flight conditions ($\mu \approx 0.189$). Under these conditions, the large wake skew angle effectively dominates over any longitudinal wake curvature effects κ_c. It is interesting to note from Table 2 that, when using the wake model of Ref. 15 which essentially neglects the implicit coupling between wake curvature and skew, the predicted absolute reduction of M_q is of the order of 9%. This is more than twice the magnitude of the effect predicted when using the modeling approach of this paper.

Accurate prediction of the off-axis pitch–roll cross-coupling derivatives (M_p and L_q) from first-principles is an issue of great current interest to the flight dynamics community. The contributing factors are predominantly aerodynamic in nature and are related to the curvature of the wake during pitching or rolling motion (Fig. 1). The effectiveness of the present approach in capturing this effect is evident from the fact that the pitch–roll cross-coupling derivatives (M_p and L_q) have been accurately predicted using $K_{Re} = 1$.

Table 1 shows that including the effect of wake curvature using the present model with $K_{Re} = 2.0$,

increases the predicted absolute values of M_p and L_q by roughly 335% and 61%, respectively. The influence of K_{Re} on the roll cross-coupling derivative M_p is significantly larger compared to that observed for the pitch cross-coupling derivative L_q. This is again attributed to the quasi-steady longitudinal wake skew angle χ which reaches 82° for $\mu \approx 0.189$. The large wake skew angle diminishes the influence of the curved wake in the longitudinal direction due to the pitching angular motion of the shaft q. This reduces the effect of wake curvature on L_q. Table 2 shows that if one neglects the aerodynamic coupling between wake curvature and skew as done in the Krothapalli model (Ref. 15), the predicted absolute increase in L_q is of the order 91%. This is 30% higher compared to predictions carried out with the present model.

A definitive conclusion cannot be reached on which mathematical model has yielded better numerical predictions with respect to the pitch-roll cross-coupling derivatives M_p and L_q. This is due to the large discrepancies noted between the identified derivatives along with the corresponding standard deviations of the overall identification process. However, from the trends observed in the numerical results produced using both models, it can be concluded that inclusion of the aerodynamic effect of wake curvature tends to improve the correlation of the predicted stability derivatives with those identified from flight test data.

Effect of dynamic wake curvature on nonlinear control response characteristics

This section investigates the effect of wake curvature on the control response of the Bo 105 helicopter. Numerical predictions are compared with flight test data reported in Refs. 27,28, as well as with nonlinear simulations carried out in Ref. 29 (Free-wake/FEA) using a high-fidelity comprehensive rotorcraft code.

The method of Ref. 29 utilizes elastically and inertially coupled modal properties derived from Finite Element Analysis (FEA) for the structural representation of the rotor blades. A relaxation-type free-wake inflow model is deployed (Ref. 30) which solves iteratively for the 3D geometry of the wake. Thus, the model resolves the effect of wake curvature numerically and also accounts for the self-induced roll-up of the blade tip vortices. The present rotor dynamics model has been adapted from Ref. 21 and does not account for elastic coupling in the employed modal properties. However, inertial coupling is retained through inclusion of the associated forcing terms in the kinematic equations of elastic blade motion. The effect of wake curvature is modeled analytically whilst the self-induced wake roll-up is not accounted for. The effects of modeling fidelity in terms of structural dynamics and wake complexity on the control response of the Bo 105 helicopter, have been extensively investigated by the author in Ref. 21.

Two control maneuvers have been selected to be simulated, each corresponding to a different set of flight conditions; near-hover ($\mu \approx 0.040$) and cruising forward flight ($\mu \approx 0.189$). The respective values of wake skew angle χ reach 45° and 82°, respectively. Figures 5(a) and (b) present the time variations of control deflections from trim as percentages of full control travel. Figure 5(a) shows that for near-hovering flight, the control schedule comprises predominantly deflections in lateral cyclic θ_{1c} with negligible pilot-induced perturbations applied to the remaining control angles (θ_0, θ_{1s}, and θ_{0tr}). Regarding the forward flight case, it can be noted from Fig. 5(b) that the control schedule includes solely deflections in longitudinal cyclic θ_{1s}. The control maneuvers shown in Fig. 5 have been extracted from Refs. 27, 28, respectively.

Figures 6 and 7 demonstrate the effect of K_{Re} on the predicted control response of the Bo 105 helicopter at near-hover flight conditions ($\mu \approx 0.040$). Numerical predictions have been carried out using the generalized wake curvature model developed in this paper and the formulation of Krothapalli (Refs. 14,15) in Figs. 6 and 7, respectively. Results are presented for the fuselage roll rate (on-axis response p) in Figs. 6 and 7(a), whilst Figs. 6 and 7(b) present the corresponding results for the fuselage pitch rate (off-axis response q). It is noted that the fuselage angular rates, through the corresponding accelerations ($\dot{p}$ and $\dot{q}$), provide an accurate indication of the unsteady moments induced by the main rotor on the fuselage.

Very good correlation, both in terms of amplitude and phase, can be observed in Figs. 6, 7(a) between analytical predictions and flight test measurements considering the on-axis response of the fuselage (roll rate p). Excellent agreement is also demonstrated between the present modeling approach and the comprehensive rotorcraft code of Ref. 29. The on-axis response is captured adequately using both the present wake curvature model (Fig. 6(a)) and the existing approach of Krothapalli (Fig. 7(a)). It can be noted that, in accordance with previous observations (Ref. 18), the effect of wake curvature on the on-axis rotor response is small, apart from the case that a large value of K_{Re} is used ($K_{Re} = 2$). The relative differences observed between predictions made with the two wake models are due to the large changes observed in the off-axis rotor response (Figs. 6, 7(b)). These are attributed to the cross-coupling characteristics of the Bo 105 helicopter rotor system (Ref. 31) that implicitly influence the on-axis behavior as well (Ref. 21).

The significance of including the effect of wake curvature becomes apparent when it comes to accurate prediction of the off-axis rotor response (pitch rate q). This is effect is clearly demonstrated in the results presented in Figs. 6, 7(b). Considering the simulations conducted excluding the aforementioned

effect ($K_{Re} = 0$), the predicted off-axis response correlates poorly with the flight test results. However, numerical predictions carried out including this effect ($K_{Re} \geq 1$) show increasingly good agreement with the measured data. This observation applies with respect to both analytical wake curvature models. Good agreement can also be noted between the present analytical model and the comprehensive rotorcraft code of Ref. 29 that resolves the curved three-dimensional wake geometry numerically (free-wake approach).

The character of the effect of K_{Re} on the off-axis rotor response is very similar for the two wake models. However, Figs. 6, 7(b) show that for a given value of $K_{Re} \neq 0$, the amplitude of the associated change in the predicted off-axis response is different between the two models. Specifically, the present approach (Fig. 6(b)) with $K_{Re} = 1.5$ correlates very well with the measurements and also with the method of Ref. 29 (Free-wake/FEA). However, in order for the Krothapalli model (Fig. 7(b)) to yield a correlation of similar quality, the required value of K_{Re} reaches approximately 2.0. Thus, for the imposed flight conditions ($\mu = 0.04$, $\chi = 45°$), the present approach predicts higher amplitude for the inflow perturbations due to the effect of a curved wake, compared to the formulation of Krothapalli. However, Fig. 4 showed that the influence of K_{Re} on the numerical behavior of both models is nearly identical for axial-flow conditions ($\mu = 0$, $\chi = 0°$). Thus, the differences observed between the two wake models are mainly attributed to the coupling of wake curvature with the wake skew angle χ which is omitted in the Krothapalli model.

The observed discrepancies between the two models may increase for certain values of advance ratio μ and wake skew angle χ. Under such conditions the Krothapalli model would require non-physically large values of K_{Re} compared to the ideal theoretical value of 1.0, in order to compensate for omitting the aerodynamic coupling between wake curvature and skew. However, such a correction would be somewhat arbitrary and not justified based on physical arguments. Furthermore, for the modest wake skew angle of the specific case study (45°), Fig. 7(b) shows that the approach of Krothapalli does not capture the maximum measured off-axis pitch rate response (p) that occurs for $t \approx 3.75sec$. This is despite using $K_{Re} = 2.0$ which is the maximum value that is physically justifiable. In contrast, Fig. 6(b) demonstrates that the present model is able to predict the maximum roll rate for $t \approx 3.75sec$ when using $K_{Re} = 2.0$. Thus, it can be concluded that the proposed approach constitutes an improved wake curvature model that mitigates the necessity for artificially large values of K_{Re}. Overall, the new method correlates very well with the measured data for $1.5 \leq K_{Re} \leq 2.0$, which are physically acceptable values according to Ref. 18.

Figures 8 and 9 present the effect wake curvature (K_{Re}) on the control response of the Bo 105 helicopter at forward flight conditions ($\mu \approx 0.189$, $\chi = 82^{\circ}$). Comparisons are carried out between flight test data and numerical predictions made using the present model (Fig. 8) as well as the method of Krothapalli (Fig. 9). It is noted that the employed control schedule comprises solely longitudinal cyclic θ_{1s} deflections (Fig. 5(b)). Concurrently, the fuselage roll rate p presented in Figs. 8, 9(a) corresponds to the aircraft's off-axis response, while the pitch rate q shown in Figs. 8, 9(b) denotes the associated on-axis response. It is emphasized that the approach of Krothapalli is strictly applicable to hovering flight only (Ref. 15). Therefore, the respective predictions have been carried out purely as a numerical experiment. To the author's knowledge, the nonlinear method of Ref. 29 has not been deployed for the analysis of the employed control maneuver (Ref. 27), hence the absence of the corresponding numerical data in Figs. 8 and 9.

As expected, it can be observed that for cruising forward flight conditions ($\mu \approx 0.189$) the effect of wake curvature (K_{Re}) on the helicopter's control response is benign compared to the near-hovering flight case ($\mu \approx 0.040$). This is due to the fact that during maneuvering flight, the curved rotor wake is quickly swept away from the rotor blades by the free-stream flow. This diminishes the wake's influence on the aerodynamic environment encountered by the rotor blades which is dominated by the free-stream velocity.

Figure 8 shows that both the on-axis (pitch rate q) as well as the off-axis response (roll rate p) of the fuselage have been accurately predicted using the present approach. However, the predictive accuracy for the on-axis response is not as good as that observed for the near-hovering case in Figs. 6 and 7. This is because the analysis includes additional modeling uncertainties related to the aerodynamic pitching moment of the fuselage and the horizontal stabilizer. These loads are naturally amplified for the forward flight case compared to near-hovering flight. This is due to the large free-stream velocity ($V \approx 41.15\, m/sec$) which is absent in hovering flight (Figs. 6 and 7). It is noted that the aerodynamic loads generated by the fuselage and the empennage have been modeled using the expressions proposed in Ref. 24.

Although the general character of the off-axis response (roll rate p, Fig. 8(a)) has been captured even without accounting for the influence of wake curvature ($K_{Re} = 0$), it can be observed that inclusion of the aforementioned effect ($K_{Re} \geq 1$) improves the predictive accuracy in terms of both amplitude and phase. Figure 9(a) shows that for the investigated flight conditions, deployment of the Krothapalli wake curvature model results only in slight differences in the predicted off-axis response compared to the

present analytical method. Furthermore, it can be noted from Fig. 9(b) that the on-axis pitch rate q also exhibits noticeable differences compared to the case where the present approach is employed (Fig. 8(b)). It is believed that the slightly modified off-axis fuselage roll rate p has inevitably affected the predicted on-axis behavior due to the substantial cross-coupling characteristics of the Bo 105 helicopter (Ref. 27).

Conclusions

This paper has described an improved analytical approach capable of modeling the effect of wake curvature on the dynamic response of helicopter rotors for flight dynamics applications. The method has been derived from first-principles and is based on a generalization of the classical vortex tube model. The overall theory has been reduced to a finite set of integral expressions that describe the inter-harmonic coupling between perturbed rotor inflow and circulatory disk loading. The derived expressions have been superimposed upon the inflow gain matrices of an existing finite-state induced flow model. The end product is an augmented rotor inflow formulation that includes the effect wake curvature and is applicable to the general case of non-zero wake skew angle. The combined method has been coupled with an unsteady blade element model, a rotor blade structural mechanics model, and a nonlinear rotor dynamics model. The integrated approach has been deployed to investigate the effect of wake curvature on the flight dynamics of a hingeless rotor helicopter. The specific conclusions drawn can be summarized as follows:

1) The proposed analytical approach is applicable to both hover and forward flight conditions. Furthermore, it retains the linear and quadratic aerodynamic coupling terms between wake curvature and skew that were omitted in previous attempts to extract the corresponding inflow perturbation coefficients.

2) The new model accounts for the inflow perturbations due to the effects of both mean and first harmonic circumferential variations of disk loading. Furthermore, it includes higher-order frequency content up to the third harmonic of rotor inflow which was omitted in previous wake curvature models.

3) The developed aerodynamic theory agrees very well with existing, non-general, vortex tube-based models for axial-flow conditions. Furthermore, the overall method improves on existing axial-flow models by including the previously omitted azimuthal variations of circulatory disk loading.

4) Accounting for the aerodynamic coupling between wake curvature and wake skew may lead to a 30% decrease in the predicted value of L_q, compared to the case where the aforementioned coupling is neglected. Inclusion of this effect improves the correlation of L_q with the identified data considerably.

5) The proposed analytical model agrees well with numerical predictions carried out through numerically resolving the complex, three-dimensional wake geometry in a nonlinear fashion.

6) The developed approach is able to accurately predict the off-axis response of a hingeless rotor helicopter at near-hover conditions using a K_{Re} value between 1.5 and 2.0. The new method predicts inflow perturbations of larger amplitude compared to previous models. This implicitly mitigates the necessity for artificially large values of K_{Re} that deviate substantially from the theoretical value of 1.0.

Hence, the proposed mathematical approach constitutes an improved finite-state induced-flow model that accounts for the curvature of the trailing wake during transient flow simulation. The developed fluid mechanics formulation is a time-accurate method that is applicable to both hover and forward flight conditions. Furthermore, the method is applicable to any open rotor system whose wake can be modeled using incompressible potential flow theory, such as wind-turbines, helicopter rotors, and low-speed propellers.

References

[1]Leishman, J., Bhagwat, M., and Bagai, A., "Free-vortex filament methods for the analysis of helicopter rotor wakes," *Journal of Aircraft*, Vol. 39, (5), September-October 2002, pp. 759–775.

[2]Brown, R. E., "Rotor Wake Modeling for Flight Dynamic Simulation of Helicopters," *AIAA Journal*, Vol. 38, (1), January 2000, pp. 57–63.

[3]Renaud, T., O'Brien, D., Smith, M., and Potsdam, M., "Evaluation of Isolated Fuselage and Rotor-Fuselage Interaction using CFD," Proceedings of the 60th Annual Forum of the American Helicopter Society, Baltimore, Maryland, USA, June 2004.

[4]Johnson, W., "A History of Rotorcraft Comprehensive Analyses," Proceedings of the 69th Annual Forum of the American Helicopter Society, Phoenix, Arizona, May 2013.

[5]Bhagwat, M. J. and Leishman, J. G., "Stability, Consistency and Convergence of Time-Marching Free-Vortex Rotor Wake Algorithms," *Journal of the American Helicopter Society*, Vol. 46, (1), January 2001, pp. 59–71.

[6]Leishman, G. J., Bhagwat, M. J., and Ananthan, S., "The Vortex Ring State as a Spatially and Temporally Developing Wake Instability," *Journal of the American Helicopter Society*, Vol. 49, No. 2, 2004, pp. 160.

[7]Horn, J. F., Bridges, D. O., A.Wachspress, D., and Rani, S. L., "Implementation of a Free-Vortex

Wake Model in Real-Time Simulation of Rotorcraft," *Journal of Aerospace Computing, Information, and Communication*, Vol. 3, (3), March 2006, pp. 93–114.

[8]Peters, D. A., Boyd, D. D., and He, C. J., "Finite-State Induced-Flow Model for Rotors in Hover and Forward Flight," *Journal of the American Helicopter Society*, Vol. 34, (4), October 1989, pp. 5–17.

[9]Peters, D. A. and He, C. J., "Correlation of Measured Induced Velocities With a Finite-State Wake Model," *Journal of the American Helicopter Society*, Vol. 36, (3), July 1991, pp. 59–70.

[10]Peters, D., "How Dynamic Inflow Survives in the Competitive World of Rotorcraft Aerodynamics," *Journal of the American Helicopter Society*, Vol. 54, (1), January 2009, pp. 1–15.

[11]Pitt., D. M. and Peters, D. A., "Theoretical Prediction of Dynamic Inflow Derivatives," *Vertica*, Vol. 5, (1), March 1981, pp. 21–34.

[12]Takahashi, M. D., "A Flight-Dynamic Helicopter Mathematical Model with a Single Flap-Lag-Torsion Main Rotor," NASA, TM 102267, USAAVSCOM TM 90-A-004, February 1990.

[13]Rosen, A. and Isser, A., "A Model of the Unsteady Aerodynamics of a Hovering Helicopter Rotor that Includes Variations of the Wake Geometry," *Journal of the American Helicopter Society*, Vol. 40, (3), July 1995, pp. 6–16.

[14]Krothapalli, K. R., Prasad, J. V. R., and Peters, D. A., "Improved Wake Geometry Model for a Maneuvering Rotor," Proceedings of the Atmospheric Flight Mechanics Conference of the American Institute of Aeronautics and Astronautics, San Diego, California, July 1996.

[15]Krothapalli, K. R., Prasad, J. V. R., and Peters, D. A., "Helicopter Rotor Dynamic Inflow Modeling for Maneuvering Flight," *Journal of the American Helicopter Society*, Vol. 46, (2), April 2001, pp. 129–139.

[16]Prasad, J. V. R., Zhao, J., and Peters, D. A., "Modeling of Rotor Dynamic Wake Distortion During Maneuvering Flight," Proceedings of the 2001 AIAA Atmosphere Flight Mechanics Conference, Montreal, Canada, August 6-9 2001.

[17]Zhao, J., Prasad, J. V. R., and Peters, D. A., "Rotor Dynamic Wake Distortion Model for Helicopter Maneuvering Flight," *Journal of the American Helicopter Society*, Vol. 49, (4), October 2004, pp. 414–424.

[18]Zhao, J., *Dynamic Wake Distortion Model for Helicopter Maneuvering Flight*, Ph.D. thesis, School of Aerospace Engineering, Georgia Institute of Technology, Atlanta, Georgia, USA, March 2005.

[19]Dress, J. M., "A Theory of Airflow Through Rotors and Its Application to Some Helicopter Problems," *Journal of the Helicopter Association of Great Britain*, Vol. 3, (2), July-September 1949, pp. 79–104.

[20]Anderson, J. D., *Fundamentals of Aerodynamics*, McGraw-Hill, Boston, 2011.

[21]Goulos, I., Pachidis, V., and Pilidis, P., "Helicopter Rotor Blade Flexibility Simulation for Aeroelasticity and Flight Dynamics Applications," *Journal of the American Helicopter Society*, Vol. 59, (4), October 2014.

[22]Goulos, I., Pachidis, V., and Pilidis, P., "Lagrangian Formulation for the Rapid Estimation of Helicopter Rotor Blade Vibration Characteristics," *Aeronautical Journal*, Vol. 118, (1206), August 2014.

[23]Leishman, J. G. and Beddoes, T. S., "A Semi-Empirical Model for Dynamic Stall," *Journal of the American Helicopter Society*, Vol. 34, (3), July 1989, pp. 3–17.

[24]Padfield, G. D., *Helicopter Flight Dynamics*, Blackwell Publishing, Oxford, England, UK, 2007.

[25]Goulos, I., Pachidis, V., and Pilidis, P., "Flexible Rotor Blade Dynamics for Helicopter Aeromechanics Including Comparisons with Experimental Data," *Aeronautical Journal*, Vol. 119, (1213), March 2015.

[26]Bramwell, A. R. S., Done, G., and Balmford, D., *Bramwell's Helicopter Dynamics*, Butterworth-Heinemann, Oxford, England, UK, 2001.

[27]AGARD, "Rotorcraft System Identification," Advisory Group for Aerospace Research and Development, AGARD LS 178, 1991.

[28]Kaletka, J. and Gimonet, B., "Identification of Extended Models from BO-105 Flight Test Data for Hover Flight Condition," Proceedings of the 21st European Rotorcraft Forum, Saint Petersburg, Russia, August 1995.

[29]Theodore, C., *Helicopter Flight Dynamics Simulation with Refined Aerodynamic Modeling*, Ph.D. thesis, University of Maryland, College Park, 2000.

[30]Bagai, A. and Leishman, J. G., "Rotor Free-Wake Modeling using a Pseudo-Implicit Technique - Including Comparisons with Experimental Data," *Journal of the American Helicopter Society*, Vol. 40, (3), April 1995, pp. 29–41.

[31]Staley, J. A., "Validation of Rotorcraft Flight Simulation Program through Correlation with Flight Data for Soft-in-plane Hingeless Rotor," USAAMRDL-TR-75-50, 1976.

Table 1. Comparison of estimated stability derivatives $(1/sec)$ with values identified from flight tests – Present wake curvature model

Derivative	AFDD (σ)	DLR (σ)	NAE (σ)	$K_{Re}=0$	$K_{Re}=1$	$K_{Re}=1.5$	$K_{Re}=2$
M_p	-0.998 (0.066)	-0.419 (0.038)	-1.414 (0.066)	**-0.632**	**-1.693**	**-2.222**	**-2.750**
M_q	-4.493 (0.235)	-3.496 (0.047)	-2.992 (0.074)	**-3.860**	**-3.777**	**-3.735**	**-3.696**
L_p	-8.779 (0.641	-8.501 (0.011)	-7.048 (0.201)	**-10.809**	**-9.281**	**-8.523**	**-7.771**
L_q	3.182 (0.624)	3.037 (0.125)	4.454 (0.222)	**2.778**	**3.6230**	**4.057**	**4.478**

Table 2. Comparison of estimated stability derivatives $(1/sec)$ with values identified from flight tests – Krothapalli wake curvature model (Refs. 14, 15)

Derivative	AFDD (σ)	DLR (σ)	NAE (σ)	$K_{Re}=0$	$K_{Re}=1$	$K_{Re}=1.5$	$K_{Re}=2$
M_p	-0.998 (0.066)	-0.419 (0.038)	-1.414 (0.066)	**-0.632**	**-0.943**	**-1.098**	**-1.255**
M_q	-4.493 (0.235)	-3.496 (0.047)	-2.992 (0.074)	**-3.860**	**-3.686**	**-3.598**	**-3.512**
L_p	-8.779 (0.641	-8.501 (0.011)	-7.048 (0.201)	**-10.809**	**-10.402**	**-10.195**	**-9.987**
L_q	3.182 (0.624)	3.037 (0.125)	4.454 (0.222)	**2.778**	**4.043**	**4.676**	**5.308**

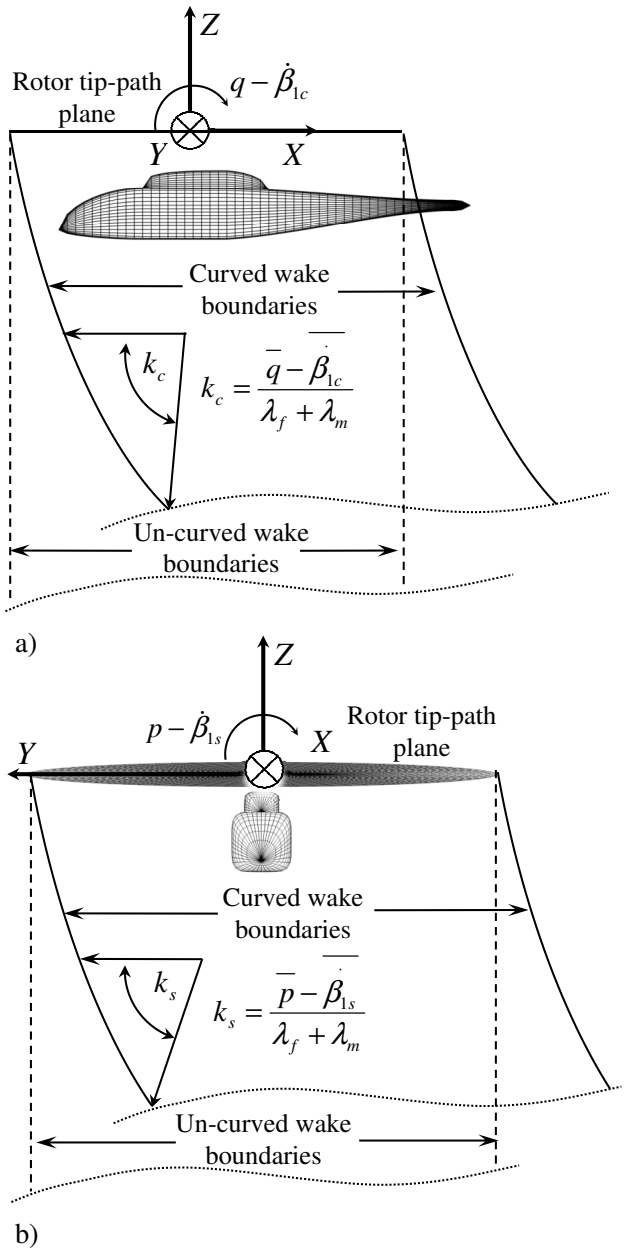

Fig. 1 Example of wake curvature during near-hover maneuvering flight (wake contraction not accounted for): (a) Longitudinal wake curvature for pitch-up maneuver, (b) Lateral wake curvature for a left-roll maneuver

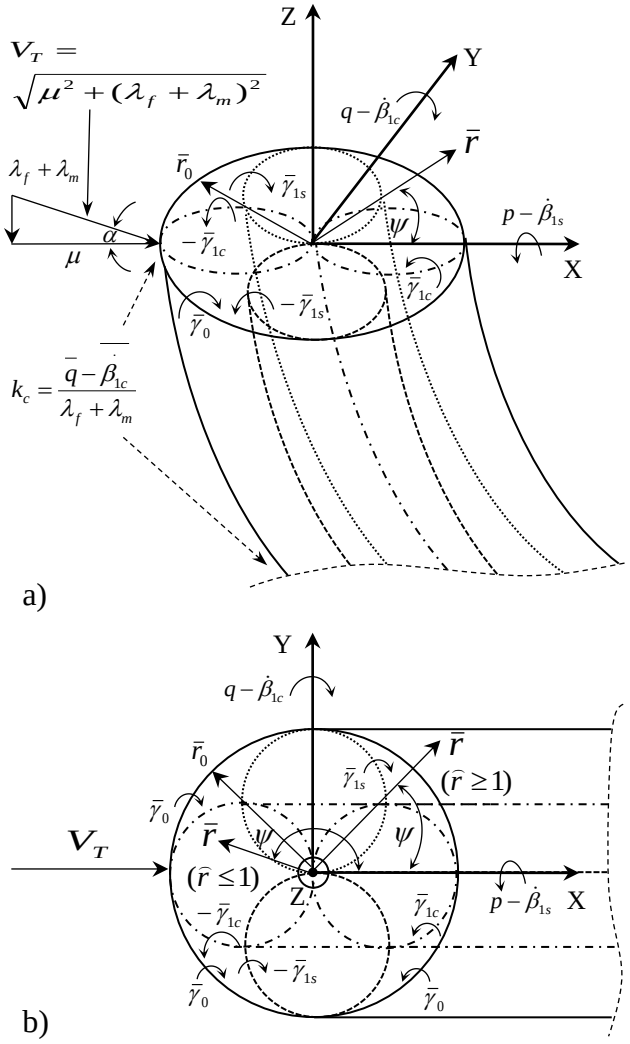

Fig. 2 Vortex tube analysis: (a) Vortex tube configuration employed for the estimation of rotor inflow perturbations due the effect of dynamic wake curvature, (b) Employed reference systems and distribution of vorticity strength

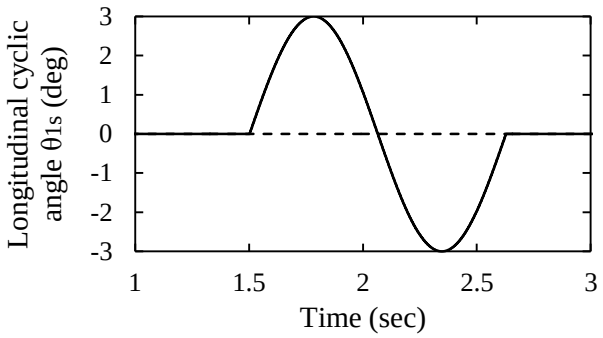

Fig. 3 Longitudinal cyclic θ_{1s} control input schedule applied to the centrally hinged articulated rotor

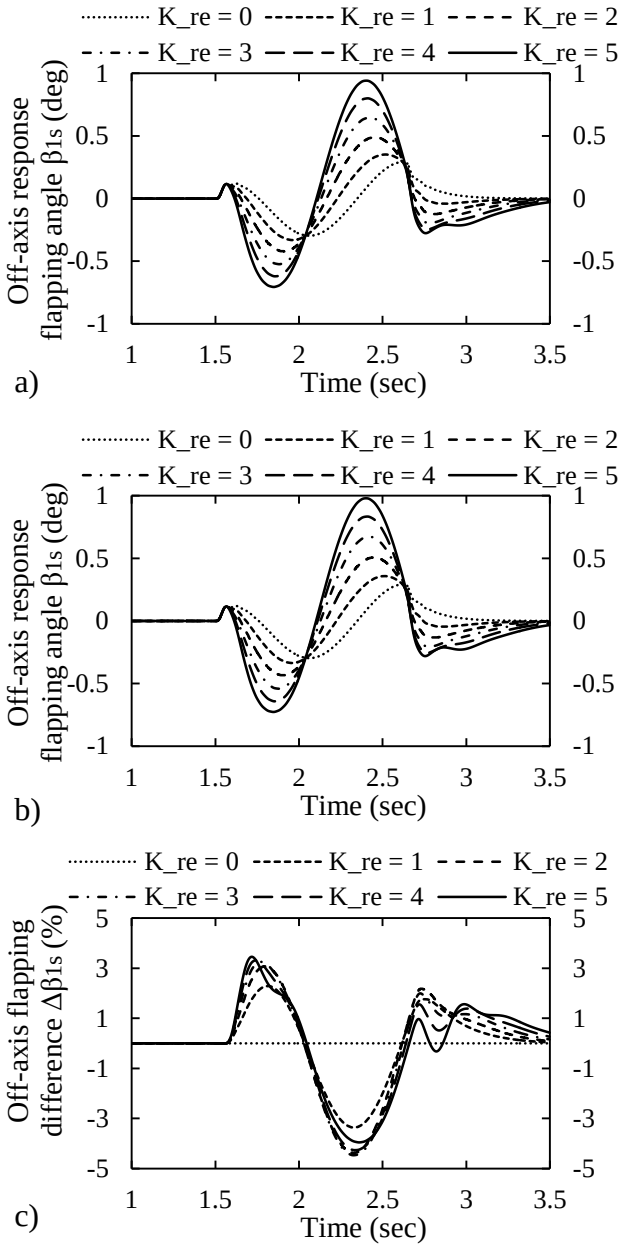

Fig. 4 Effect of wake curvature parameter K_{Re} on the off-axis flapping response β_{1s} of the dynamically neutral articulated rotor, $\mu = \lambda_f = 0$, Number of flow-states = 62: (a) Present wake curvature model, (b) Krothapalli wake curvature model (Refs. 14, 15), (c) Percentage differences between the two models

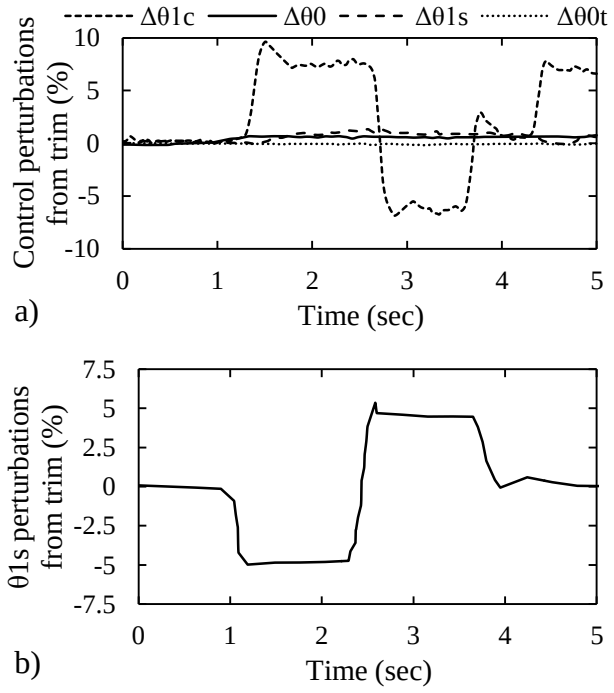

Fig. 5 Control perturbations from trim: (a) Near-hover maneuver; $\mu \approx 0.040$, (b) Forward flight maneuver; $\mu \approx 0.189$ (changes are applied on longitudinal cyclic θ_{1s} only)

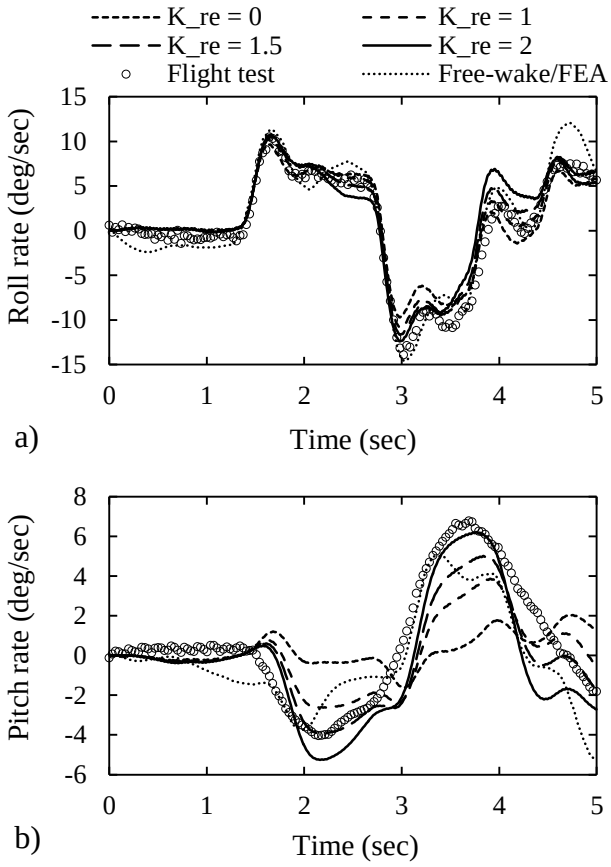

Fig. 6 Effect of wake curvature parameter K_{Re} on the predicted control response of the Bo 105 helicopter at near-hover flight conditions, $\mu \approx 0.040$, Present wake curvature model: (a) Fuselage roll rate (on-axis response), (b) Fuselage pitch rate (off-axis response)

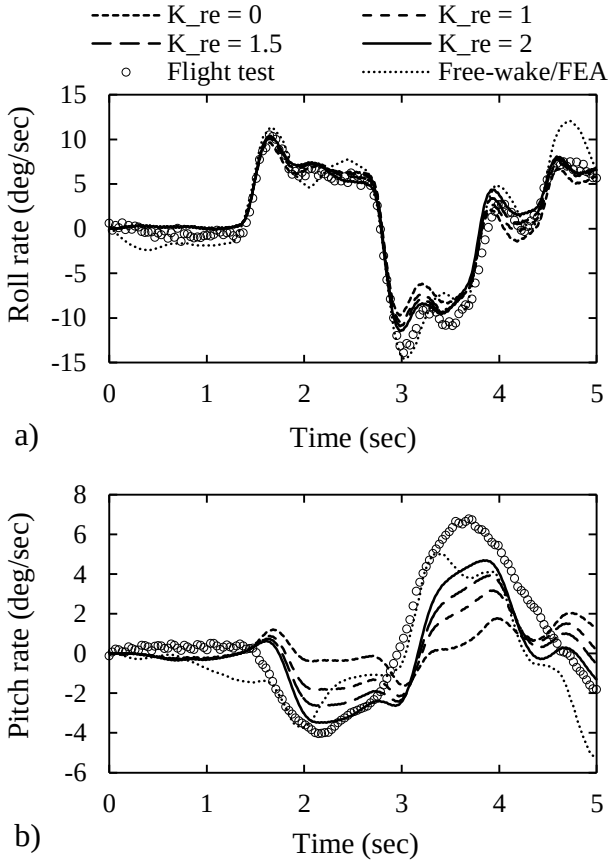

Fig. 7 Effect of wake curvature parameter K_{Re} on the predicted control response of the Bo 105 helicopter at near-hover flight conditions, $\mu \approx 0.040$, Krothapalli wake curvature model (Refs. 14, 15): (a) Fuselage roll rate (on-axis response), (b) Fuselage pitch rate (off-axis response)

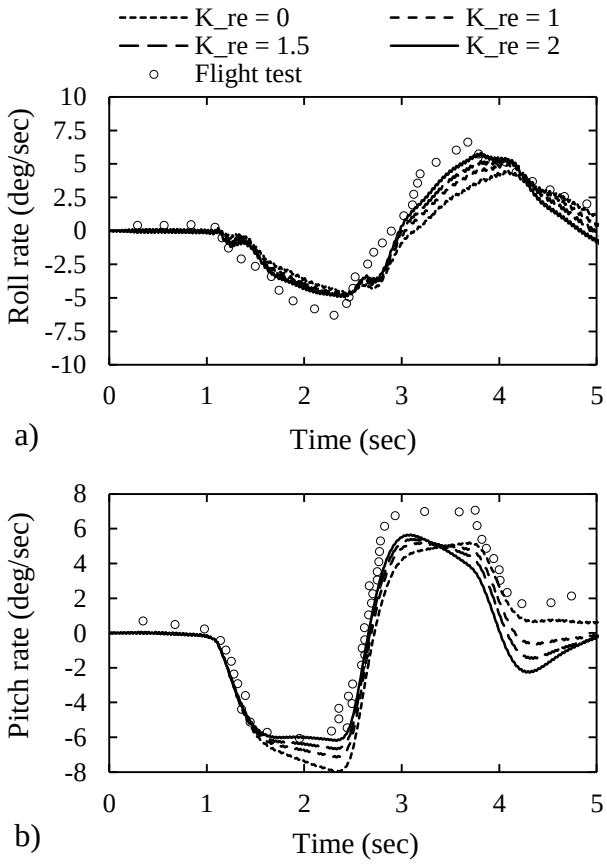

Fig. 8 Effect of wake curvature parameter K_{Re} on the predicted control response of the Bo 105 helicopter at forward flight conditions, $\mu \approx 0.189$, Present wake curvature model: (a) Fuselage roll rate (off-axis response), (b) Fuselage pitch rate (on-axis response)

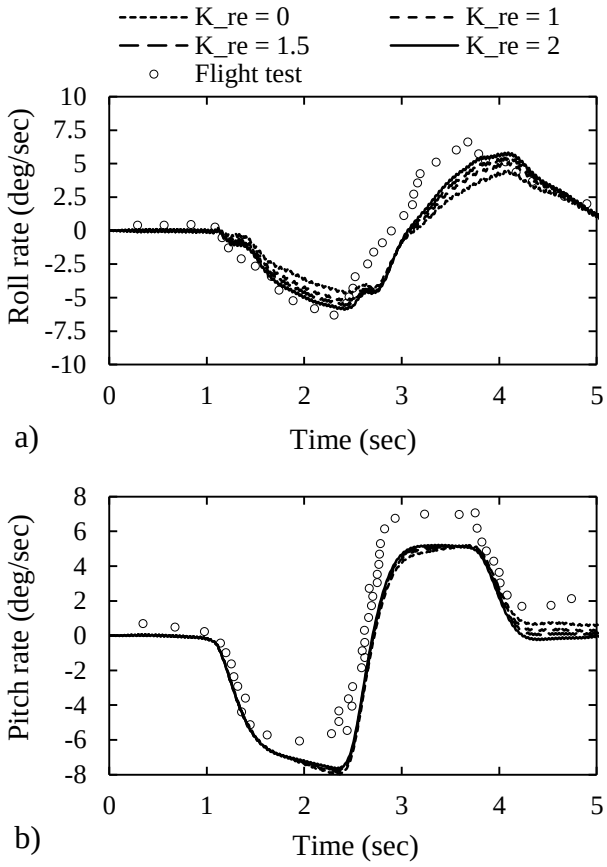

Fig. 9 Effect of wake curvature parameter K_{Re} on the predicted control response of the Bo 105 helicopter at forward flight conditions, $\mu \approx 0.189$, Krothapalli wake curvature model (Refs. 14, 15): (a) Fuselage roll rate (off-axis response), (b) Fuselage pitch rate (on-axis response)

https://dspace.org/

An improved analytical approach for modeling the effect of rotor wake curvature using finite-state induced flow models

Goulos, Ioannis

2016-07-01
Vertical Flight Society
https://doi.org/10.4050/JAHS.61.032010
Goulos I. (2016) An improved analytical approach for modeling the effect of rotor wake curvature using finite-state induced flow models. Journal- American Helicopter Society, Volume 61, Issue 3, July 2016, pp. 1-16

Downloaded from a DSpace repository. https://dspace.org/